

**FACULTY
OF MATHEMATICS
AND PHYSICS**
Charles University

MASTER THESIS

Lucia Kapitánová

**Study of the time-dependent CP
violation at the Belle II experiment**

Institute of Particle and Nuclear Physics

Supervisor of the master thesis: Mgr. Radek Žlebčík, Ph.D.

Study programme: Physics

Study branch: Nuclear and Subnuclear Physics

Prague 2021

I declare that I carried out this master thesis independently, and only with the cited sources, literature and other professional sources. It has not been used to obtain another or the same degree.

I understand that my work relates to the rights and obligations under the Act No. 121/2000 Sb., the Copyright Act, as amended, in particular the fact that the Charles University has the right to conclude a license agreement on the use of this work as a school work pursuant to Section 60 subsection 1 of the Copyright Act.

In date

Author's signature

First and foremost, I would like to express special gratitude to my supervisor Radek Žlebčík, and my consultant Jakub Kandra for their professional advice, guidance and patience over the past two years. Their help and willingness to discuss not only topics covered in this work, but also other issues encountered on the way to its completion, made this analysis and thesis possible.

Second, I would like to extend my sincere gratitude and appreciation to Zdeněk Doležal, who gave me the opportunity to participate at the Belle II experiment.

Furthermore, I want to thank all the members of the Prague Belle II group and the MPI group from Munich for their insightful comments, valuable suggestions and experience which they were kind enough to share with me to help me better understand the topic of proper time resolution function and analysis of the time-dependent CP violation.

Last but not least my gratitude belongs to my parents and friends, Chris, Teddy, Eliška, Zuzana and Pavel for their unwavering support during every stage of my studies.

Title: Study of the time-dependent CP violation at the Belle II experiment

Author: Lucia Kapitánová

Institute: Institute of Particle and Nuclear Physics

Supervisor: Mgr. Radek Žlebčík, Ph.D., Institute of Particle and Nuclear Physics

Abstract: This thesis is devoted to studies of the proper decay-time resolution function and particle decay vertex reconstruction tools, their applicability and role in the studies of time-dependent CP violation at the Belle II experiment. A positive effect of beam spot constraints and new beam spot calibration on the vertex reconstruction precision is seen via MC/data comparison. The core part of the work focuses on studying universality of the time resolution function across nine different neutral and charged B -meson decay channels. The possibility to use a single form of this function for all studied channels is demonstrated and supported by the consistency between the lifetime values used for simulation and obtained as results of the decay time difference fit.

Keywords: Time-dependent CP violation calibration B-mesons

Contents

Introduction	3
1 SuperKEKB & Belle II	5
1.1 Timescale in a nutshell	5
1.2 SuperKEKB	6
1.3 Belle II detector	6
1.3.1 Vertex Detector - VXD	7
1.3.2 Pixel Silicon Detector - PXD	7
1.3.3 Silicon Vertex Detector - SVD	8
1.3.4 Central Drift Chamber - CDC	8
1.3.5 Particle Identification Detectors	8
1.3.6 Aerogel Ring Imaging Cherenkov Detector	8
1.3.7 Time of Propagation Detector - TOP	8
1.3.8 Electro-magnetic Calorimeter - ECL	9
1.3.9 $Kaon_L$ and Muon Detector	9
1.3.10 The Trigger System	9
1.3.11 The Data Acquisition System - DAQ	9
1.3.12 The Belle II Analysis Software Framework - basf2	9
2 CKM matrix and Belle II	11
2.1 CP asymmetries	12
2.2 Mixing frequency - flavor oscillations	14
2.3 Proper Decay-Time Difference	14
2.4 Time resolution function	16
3 MC/Data validation of vertex tagging constraints	20
3.1 GRID and remote data processing	20
3.2 BeamSpot Calibration	20
3.3 Tag-side Vertexing Constraints	21
3.4 Validation - MC/Data comparison	22
3.4.1 MC and Data Samples	22
3.4.2 Summer 2020 Monte Carlo and Data Tag-side Vertexing Constraint Validation	23
3.4.3 Fall 2020 Monte Carlo and Data Comparison - Tag-side Vertexing Constraint and BeamSpot Calibration Validation	25
4 Resolution Function Studies	30
4.1 Belle II Resolution Function	30
4.2 Technical Details	30
4.2.1 Variables and Important Relations	30
4.2.2 Older MC Sample	31
4.2.3 New MC Dataset	32
4.2.4 Kinematic Approximation	32
4.2.5 Form of the Resolution Function	33
4.2.6 Time Resolution and Lifetime Studies in Steps	33

4.3	Results	34
4.3.1	MC processed before Summer 2020	34
4.3.2	Preliminary Studies	34
4.4	Time Resolution Function and Lifetime Fit - Results	35
4.4.1	B0toPiDPtoK2Pi	37
4.4.2	B0toPiDStoK2Pi	39
4.4.3	B0toPiDStoK4Pi	41
4.4.4	B0toJPsiKStoMuMu	43
4.4.5	B0toJPsiKStoEE	45
4.4.6	BPtoJPsiKtoMuMu	47
4.4.7	BPtoJPsiKtoEE	49
4.4.8	BPtoPiD0toKPi	51
4.4.9	BPtoPiD0toK3Pi	53
4.4.10	Preliminary Results - New MC Dataset	55
5	Discussion	56
	Conclusion	62
	Bibliography	63
	List of Figures	66
	List of Tables	67
A	Time Resolution Function and Lifetime Fit - Summary Table	68

Introduction

The imperfections of the Standard Model (SM) supply scientists with a cornucopia of intriguing questions. Despite the fact that the SM has proven to be a model successful at describing many aspects of the microscopic world, our understanding of the fundamental laws of nature is not complete. Attempts are made to refute the predictions made by the Standard Model in order to explain deeper underlying mysteries, such as e.g. matter-antimatter asymmetry observed in the universe, which the Standard Model fails to elucidate.

For the phenomena of baryogenesis to occur, three conditions were formulated by Andrei D. Sakharov, Russian physicist [1, 2, 3]. One of these conditions asks for violation of charge-parity (CP) symmetry, which was long believed to be preserved.

With the evolution of experimental technology, the charge-parity violation was indeed measured in weak interactions [4] and become a fruitful topic also for the theoreticians. Theoretical physicists Kobayashi and Maskawa came up with a way how to naturally incorporate the description of this phenomenon into the SM if the number of quark flavors proved to be six [3]. At the time of their proposal, three more quark flavors were left to be experimentally discovered, and confirmed [3]. Once their existence was measured, the Cabibbo-Kobayashi-Maskawa (CKM) matrix was adopted as an essential part of the current form of the Standard Model.

The CKM matrix is a 3x3 complex unitary matrix describing the mixing of quark flavors in weak interactions, parametrized by three mixing angles and one irreducible Kobayashi-Maskawa complex phase, which characterizes the CP violation [5].

In order to verify their proposition, the matrix elements must be precisely measured. The CKM matrix can be represented geometrically employing unitarity triangles [2]. The task of testing the ability of the matrix to describe CP-violating effects present at the level of the SM then comes down to over-constraining the angles and side lengths of these triangles. Moreover, the extent of the CP violation, which gets introduced through the CKM matrix, is insufficient to fulfill Sakharov's condition. Therefore, there is a reason to believe further CP violation could be found in processes and phenomena extending the scope of the SM in the areas of New Physics [6].

Not only Physics beyond the Standard Model has become a driving force in rapid experimental development in the field of particle physics. One of the most efficient experimentally accessible playgrounds for CP-violation measurements is the system of B mesons oscillating between a particle-antiparticle state. Advances in this area have been achieved at the specialized asymmetric accelerating facilities, so-called B-factories [7], explicitly built for this purpose.

A member of this group, the Belle II experiment [8] operating at the SuperKEKB e^+e^- collider with asymmetric beam energies attacks the B-sector CP violation measurements at the precision frontier through the $\Upsilon(4S) \rightarrow B\bar{B}$ decay chain [9]. This experiment, following in the footsteps of other B factories such as BaBar [10] operated at PEP-II accelerator at SLAC and Belle [11] at the KEKB accelerator at KEK, does not limit its physics program solely to CP-violation

studies. The collaboration consists of nine working groups focused on exploring the realms of B physics, but also *charm* and τ quark and quarkonia physics, electroweak precision measurements, and search for the dark sector physics [6]. Out of these working groups, the group handling the "Time-dependent CP violation" (TDCPV) exploration will be of particular interest throughout this thesis.

The asymmetric nature of the SuperKEKB collider provides the neutral B -meson pair with a relativistic boost. This way, the possibility of studying time-dependent CP asymmetry and violation-related parameters is unlocked. Special attention will be paid to the proper time resolution function [2, 3, 12] essential to precise measurement of the B -meson lifetime τ_B , the Unitarity triangle angles, $B^0\bar{B}^0$ oscillation frequency [6]. This function links together the experimental limitations such as detector effects and resolution and event reconstruction precision with the physical distributions and measured values of the variables of interest. Their relationship can be represented as follows [3]:

$$\mathcal{F}(\Delta t) = \int P_{sig}(\Delta\bar{t})\mathcal{R}(\Delta t - \Delta\bar{t})d(\Delta\bar{t}) \quad (1)$$

where Δt represents the difference between proper decay times of both B mesons, P_{phys} describes the theoretical physical probability distribution function of the variable, and \mathcal{R} is the studied resolution function. Precisely the proper time-resolution function and other aspects of time-dependent CP analysis will be the main subject of interest of this work, the structure of which is organized as follows.

The first chapter introduces the upgraded research facility SuperKEKB, the Belle II experiment, and briefly summarizes the key components of the Belle II detector.

The second chapter offers a theoretical introduction to the studies of time-dependent CP violation and asymmetry in the B sector and gives a brief overview of the results achieved by prior B-factory measurements. The proper-time resolution function is introduced in this section.

The third chapter describes the author's contribution to the validation of the vertexing constraints and beam-spot calibration tools and data processing for the needs of the TDCPV working group analysis. Results of MC-Data comparison studies for hadronic B meson decay channels are presented and compared with similar studies performed in summer 2020.

The fourth chapter focuses on the studies of universality of the introduced form of time resolution function and its applicability to fitting all nine studied decay modes. This form of the function is used for the determination of B -meson lifetime values.

In Chapter 5, the presented results are discussed, and possible improvements and follow-up studies are presented.

1. SuperKEKB & Belle II

As one of the world's major B factories, the SuperKEKB accelerator facility, and the Belle II experiment set out on a journey to collect a data sample of 50 ab^{-1} during its operation [6]. The detector started taking data from the electron-positron collisions producing the $\Upsilon(4S)$ in March 2019.

1.1 Timescale in a nutshell

The data-taking period, called Phase 3, was preceded by two dedicated commissioning phases.

Phase 1, referred to as The Accelerator Commissioning Phase, took place in 2016 and lacked final focusing magnets and was performed without the detector.

Later, in the period between February 2018 - July 2018, during Phase 2, the Belle II detector, instrumented with radiation monitors and one part of the vertex detector, managed to gather approximately 0.5 fb^{-1} used for specialized studies [6].

The Phase 3 data taking ongoing since 2019 [13] uses fully assembled detector and has the possibility to explore wider range of center of mass energies. Beside running at the energy corresponding to the $\Upsilon(4S)$ resonance, physics programs at $\Upsilon(1S)$ - $(6S)$ are also viable and intriguing options. [8, 14] As of May 19th, 2021 $\int \mathcal{L}_{\text{recorded}} dt = 154.09 \text{ fb}^{-1}$ of data has been collected during the Phase 3 data taking period [15].

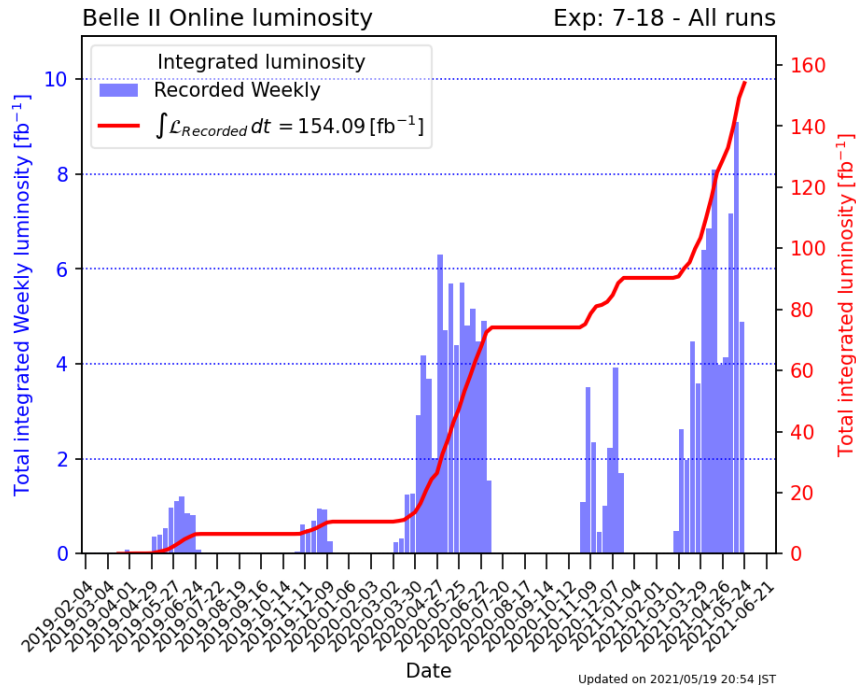


Figure 1.1: Phase 3 -Total recorded integrated luminosity as until the 19th of May, 2021[15]

1.2 SuperKEKB

The overall luminosity target is equivalent to 55 billion $B\bar{B}$ pairs, 47 billion $\tau^+\tau^-$ pairs, and 65 billion $c\bar{c}$ states [14]. In order to achieve ~ 40 times the recorded peak luminosity of KEKB, as successors of the successful Belle experiment at KEKB B-factory, the facility, and the experiment detector had to undergo significant upgrades. [14]

The SuperKEKB electron-positron accelerator running at the $\Upsilon(4S)$ resonance energy uses the tunnel initially used by its predecessor – KEKB.

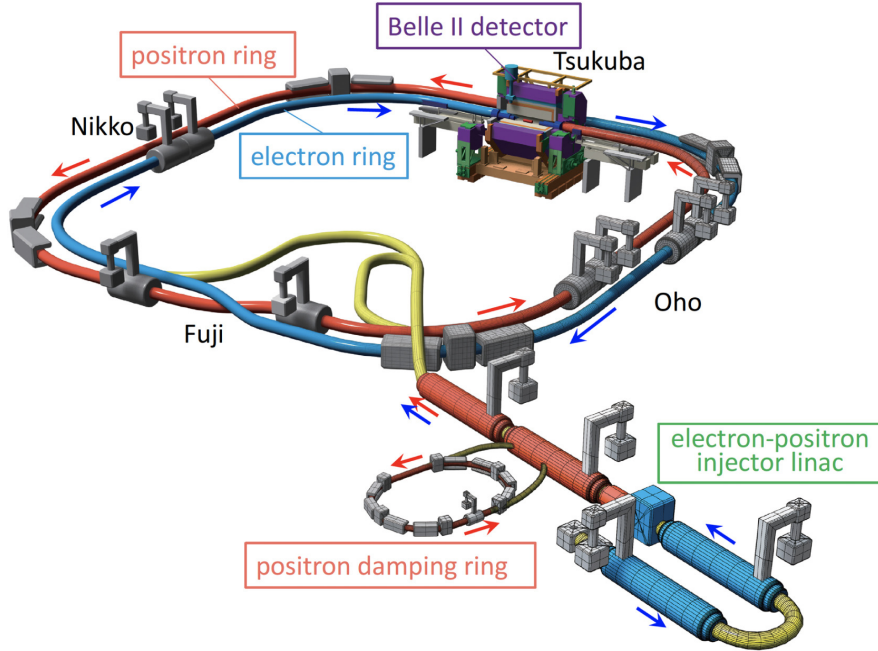


Figure 1.2: Schematic illustration of the accelerator and the Belle II detector [16]

Several steps were taken to achieve higher luminosity: The main modification is based on the so-called "Crab-Waist" scheme of collisions. In terms of the crossing angle θ , the Crab-waist scheme [17] means that $\sin\theta \ll \frac{\sigma_x}{\sigma_z}$ where $\sigma_{x(z)}$ are bunch beam sizes in corresponding directions. SuperKEKB therefore incorporated a larger crossing angle of the particle beams at the interaction point (IP), and the beam size at the IP was reduced from $1 \mu\text{m}$ to 50 nm , and the beam currents were doubled. Using large focusing magnets allows to obtain low emittance and very small vertical β_y^* function [6, 17]. Energies of the beams were also altered from 8 GeV in the electron high energy ring (HER) and 3.5 GeV in the positron low energy ring (LER) to 7 GeV and 4 GeV, respectively [6]. This modification helps reduce beam loss due to Touschek scattering in LER but also provides for a smaller boost $\beta\gamma \sim 0.28$ of the center of mass frame [8, 14].

1.3 Belle II detector

The Belle II detector, the key component to a successful physics exploration at the precision frontier, faces high levels of beam-related background radiation and high event rates. These demanding conditions required modifications and

upgrades of the previously used technology. The overall detector setup follows in the footsteps of the familiar structure of the Belle detector. However, in order to unveil the conditions present at the interaction point, it has to be equipped with completely new or revamped and ameliorated components.

The detector consists of a newly designed cylindrical vertex detection system (VXD) comprised of a pixel detector (PXD) and a double-sided silicon strip detector (SVD). The vertex detector is surrounded by a gas filled central drift chamber (CDC) followed by an innovated particle identification system (PID) consisting of an aerogel ring imaging Cherenkov detector (ARICH) in the end-caps and a time of propagation detector (TOP) covering the barrel region. Together with the K_L and μ identification system and electromagnetic calorimeter (ECL), the detector set-up is complete[8, 14]. The Belle II detector uses a right-handed, Cartesian coordinate system [18]. Its origin coincides with the location of the nominal interaction point. As shown in Figure 1.3, the horizontal z -axis, parallel with the magnetic field of the solenoid, points in the forward direction of the boost. The xy plane is orthogonal to the direction of z in such a way that the y axis points vertically upwards, and the x axis is used to describe the radial coordinate [18].

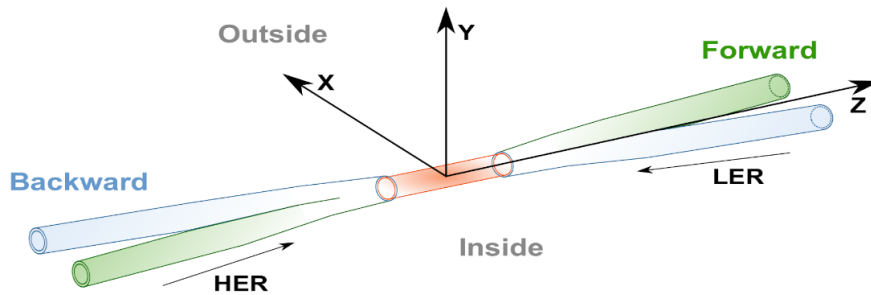


Figure 1.3: The Belle II detector Coordinate System [18]

1.3.1 Vertex Detector - VXD

To detect products and study the details of the electron-positron collisions, the vertex detector was built as close to the interaction point (IP) as possible.

1.3.2 Pixel Silicon Detector - PXD

Precise tracking and reconstruction of created charged particle trajectories rely heavily on the innermost part of the detector located closest to the interaction point - the silicon pixel detector. Two concentric layers divided into two half-shells form the cylindrical body of the PXD. These half-shells are further divided into so-called "ladders", and each of the ladders into two thin pixel silicon sensors equipped with modern DEPLETED Field Effect (DEPFET) technology. This assembly surrounds the beryllium beam pipe from a radius as small as 14 mm. The second layer of the PXD is placed within a 22 mm radius from the IP, and despite being designed to consist of twelve ladders altogether, only two are currently being used. [8, 19, 20]

1.3.3 Silicon Vertex Detector - SVD

Four concentric layers surrounding the PXD are formed by double-sided silicon strip detectors. The first SVD layer is separated from the PXD by a 16 mm gap [8]. Sensors organized into ladders form a wind-mill structure. In the central barrel part of the detector, the sensors are of a rectangular shape. On the other hand, the slanted forward region consists of trapezoidal sensors. The silicon vertex detector with its large solid angle (17 - 150 degrees) coverage [8] plays a crucial role in decay vertex reconstruction by providing information necessary for extrapolation of the tracks reconstructed in other parts of the detector (namely CDC described in the next section) to the pixel part of the detector. It also contributes to the K_s reconstruction by detecting low p_T tracks [8, 14].

1.3.4 Central Drift Chamber - CDC

The Belle II central drift chamber serves as the main tracking tool able to reconstruct a full 3D particle track helix and handle the increased background and event rates resulting from higher luminosity. The CDC can precisely determine particle momenta and identify them based on energy deposition in its volume. The CDC is a chamber filled with a 50:50 He-C₂H₆ gas mixture and comprises of more than 14 000 wires arranged into 56 layers in either the axial (parallel with the orientation of the magnetic field) or the stereo orientation (skewed with respect to the mentioned direction) [8]. In comparison with the version adapted at Belle, the current CDC is, just like the vertex detector, larger in volume, however, it consists of smaller cells. [3, 14]

1.3.5 Particle Identification Detectors

Two different sub-detector systems are used for particle identification.

1.3.6 Aerogel Ring Imaging Cherenkov Detector

In the forward end-cap region, this responsibility lays on the aerogel ring imaging Cherenkov (ARICH) detector [8] helping the detector resolution by providing two layers of aerogel, each with a different refraction index. High precision in distinguishing between kaons and pions in most of the detected momentum spectrum and is the desired characteristics of the ARICH detector [8, 14].

1.3.7 Time of Propagation Detector - TOP

In the barrel region, the particle identification based on the Cherenkov photons detection is done by the time of propagation (TOP) detector [8]. This sub-detector is formed by 16 modules, each consisting of two quartz bars, a prism, a mirror and a photo-detector. High-critical angles at the air-bar interface are the key component for photon detection.

The TOP sub-detector is able to detect the photons created by a passing of a charged particle through the radiators and provide three-dimensional information based on time of arrival and impact position of the photon [8]. Augmented

characteristics of the upgraded TOP detector could be of a special importance to two B decay channels in particular : $B \rightarrow \pi\pi$ & $B \rightarrow \rho\pi$ [3, 14].

1.3.8 Electro-magnetic Calorimeter - ECL

As many neutral particles further decaying into photons are produced in the collision, the ECL was implemented. Segmented into three parts (the forward and backward end caps and central barrel region), the ECL takes care of highly efficient and precise detection of photons over a broad energy spectrum [3]. It also participates in luminosity measurement and separation of electrons and hadrons. The Belle II electro-magnetic calorimeter consists of 8 736 CsI(Tl) scintillation crystals [8]. The Thallium-doped crystals, as well as some other parts of the machinery, are reused from the Belle detector. However, the electronics and reconstruction software are brand new and adjusted to the needs of the current detector performance[14].

1.3.9 $Kaon_L$ and Muon Detector

Outside of the superconducting solenoid 1.5 T magnetic field [8] the KLM system of the Belle II detector identifies long-living neutral Kaons and little-interacting muons with high efficiency, purity and good angular resolution. The KLM detector, divided into barrel and end-cap regions, comprises of alternating layers of active detector units and iron plates [14]. The iron layers serve as a medium for hadronic shower formed by neutral Kaons, which would otherwise fly out unnoticed by other parts of the detector. [3, 14]

1.3.10 The Trigger System

For the Belle II analysis, a highly efficient trigger system [8] is inevitable once it comes to identifying and reconstructing hadronic events from the $\Upsilon(4S) \rightarrow B\bar{B}$ and continuum [14]. The experiment's broad Physics program requires many different tailored trigger settings. Each of the sub-systems is equipped with its own information collecting sub-trigger [8]. Based on a combination of all received inputs, a trigger decision is made [3].

1.3.11 The Data Acquisition System - DAQ

The data recorded by the detector are read out by the data acquisition (DAQ) [8] system based on a signal from the trigger system. The information gathered from the front-end read-out electronics then passes through data processing to the storage system. The Belle II DAQ system has to handle a high trigger rate and keep the processing time low to avoid deadtime and, therefore, loss of luminosity [8, 21].

1.3.12 The Belle II Analysis Software Framework - basf2

The collected and stored Belle II data are subsequently processed and analyzed using the Belle II Analysis Software Framework - basf2 [22]. It is a C++/Python

based framework which individually handles each of the events by means of algorithms called "modules". Sequential combination of such modules also allows for track fitting, vertex reconstruction, or nTuple creation and the framework also serves as a simulation environment [22, 23].

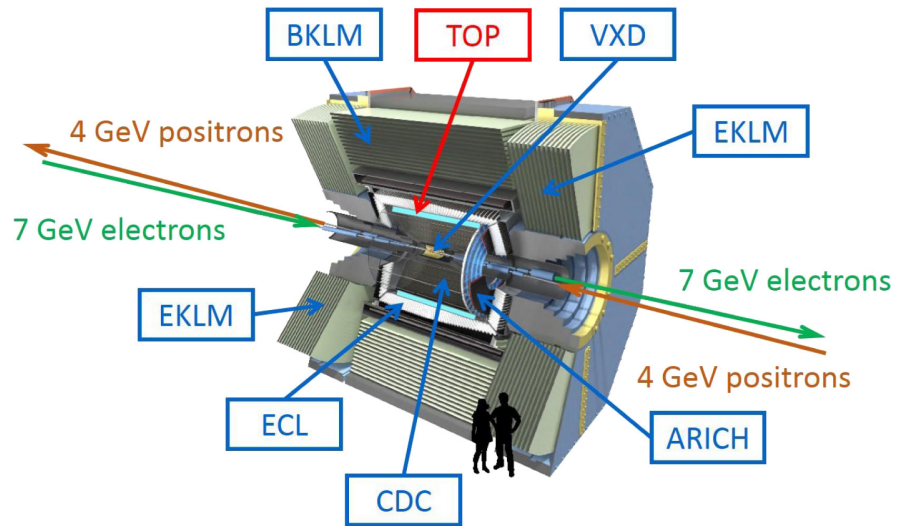


Figure 1.4: The Belle II detector [24]

2. CKM matrix and Belle II

The unitary Cabibbo-Kobayashi-Maskawa (CKM) matrix [25] describes flavor changing interactions of the Standard Model.

The unitarity requirement gives us a total of nine equations, six of which are usually visualized with a help of so-called Unitarity triangles with common area [5]. One of such triangles, Figure 2.1, is directly connected with the physics program of B-meson factories and it is described by the following equation [3, 9]:

$$\sum_i V_{id}V_{ib}^* = 0 \quad (2.1)$$

where the V_{ij} are elements of the CKM matrix related to the transition between flavors j and i . The lengths of the triangle sides are directly related to the branching fractions of B-meson decays. Together with the measurements of the triangle angles, within this thesis referred to as ϕ_1, ϕ_2 and ϕ_3 [5], they help determine the area of the triangle in a complex plane to which all the CP-violation related parameters are proportional. Non-vanishing area of the Unitarity triangle indicates the presence of the charge-parity symmetry (CP) violation [26].

The ϕ_1 angle for which it holds [5]:

$$\phi_1 \equiv \arg \left[-\frac{V_{cb}^*V_{cd}}{V_{ub}^*V_{ud}} \right] \quad (2.2)$$

can be measured through studies of the time-dependent CP violation. Systems of B mesons are considered to be the perfect ground for testing and determining the CP violation and asymmetry effects.

The tree level $b \rightarrow c\bar{c}s$ transition within one of the golden channels $B^0 \rightarrow J/\psi K_s$ and $b \rightarrow q\bar{q}s$ for $q = u, b, c$ loop diagram transitions are ideal candidates for such studies providing clear environment with relatively low background [3, 2].

The quantum-entangled $B^0\bar{B}^0$ pairs are produced in the asymmetric positron-electron collisions through the production of $\Upsilon(4S)$ resonance. They evolve over time as a correlated pair, coherently oscillating between B^0 and \bar{B}^0 states until the decay of one of the mesons collapses the wave function describing the B-meson system. The second meson keeps on oscillating with frequency Δm_d between the particle and anti-particle state.

The decay vertices of both B-mesons are reconstructed - one fully and one partially. For the B (B_{tag} or tag B), which is in general not fully reconstructed, the flavor state is always considered. Due to Bose symmetry, the other meson, referred to as signal- B or B_{sig} , has to be of the opposite flavor at the time of the decay [3, 6]. This signal B meson is reconstructed fully, and depending on whether it decays into a CP or a flavor eigenstate, the event can be used for CP -asymmetry (B_{tag} decays to a flavor and B_{sig} to a CP eigenstate) of flavor-mixing studies (both B s decay into flavor eigenstates), correspondingly [6, 9].

2.1 CP asymmetries

The daughter particles are used to determine the flavor of the B_{tag} , while the other meson, B_{sig} , is fully reconstructed in a CP eigenstate with eigenvalue $\eta_{CP} = \pm 1$.

contributions respectively, are usually represented by the A and S factors in the following way [3]:

$$\begin{aligned} S &= \frac{2Im\lambda}{1 + |\lambda|^2} \\ -A &= \frac{1 - |\lambda|^2}{1 + |\lambda|^2} \end{aligned} \quad (2.5)$$

In general, for the $b \rightarrow c\bar{c}s$ decay transitions, the factor λ takes on a form [3]:

$$\lambda = \eta_{CP} \exp -2i\phi_1 \quad (2.6)$$

The B_{sig} decay rate thus yields [3]:

$$f_{\pm}^{CP}(\Delta t; \tau_B, \Delta m_d, w, \sin 2\phi_1) = \frac{\exp -\frac{|\Delta t|}{\tau_B}}{4\tau_B} [1 \mp \eta_{CP} \mathcal{D} \sin 2\phi_1 \sin(\Delta m_d \Delta t)] \quad (2.7)$$

The above derivation applies to the idealistic case of perfect flavor determination and vertex reconstruction. In reality, the detector resolution is reckoned in by a convolution of the time-dependent decay rate distribution with a time resolution function $\mathcal{R}(\Delta t_{res})$ (see the following chapter) [2]:

$$\mathcal{F}_{\pm}(\Delta t, ; \tau_B, \Delta m_d, w, \sin 2\phi_1) = f_{\pm}(\Delta t; \tau_B, \Delta m_d, w, \sin 2\phi_1) \otimes \mathcal{R}(\Delta t_{res}) \quad (2.8)$$

An experimentally measurable variable which can be used for CP violation measurements, time-dependent asymmetry, representing the signal B meson's decay into a CP eigenstate can be defined through asymmetry between the factors \mathcal{F}_+^{CP} and \mathcal{F}_-^{CP} :

$$\begin{aligned} \mathcal{A}_{CP}(\Delta t) &= \frac{\mathcal{F}_+^{CP}(\Delta t) - \mathcal{F}_-^{CP}(\Delta t)}{\mathcal{F}_+^{CP}(\Delta t) + \mathcal{F}_-^{CP}(\Delta t)} \\ &= S \sin \Delta m_d \Delta t + A \cos \Delta m_d \Delta t \end{aligned} \quad (2.9)$$

As indicated by the expression (2.6), in the case of the golden $B^0 \rightarrow J/\psi K_s$ channel the $A \simeq 0$ and the S is directly related to the desired CKM ϕ_1 angle by $S \simeq -\eta_{CP} \sin(2\phi_1)$. The value of the $\sin 2\phi_1$ parameter can be obtained through the means of maximized likelihood function [2]:

$$\begin{aligned} \ln \mathcal{L}_{CP} &= \sum_i^{tag} [\sum_{B^0 tag} \ln \mathcal{F}_+(\Delta t; \tau_B, \Delta m_d, w_i, \sin 2\phi_1) \\ &\quad + \sum_{\bar{B}^0 tag} \ln \mathcal{F}_-(\Delta t; \tau_B, \Delta m_d, w_i, \sin 2\phi_1)] \end{aligned} \quad (2.10)$$

summer over all tagging modes. The Δt stands for the time difference in the B meson decay times.

2.2 Mixing frequency - flavor oscillations

The mixing frequency of the flavor oscillations can be determined with the use of events where one of the neutral B mesons, the signal B (B_{sig}), is reconstructed fully in a flavor eigenstate and the flavor of the tag B meson is determined by its daughter particles (just like in the case of the CP asymmetry measurements). [2]

The information of the B_{sig} meson's flavor at the time of the B_{tag} decay allows for the determination of probabilities for finding different flavor pairs ($B^0\bar{B}^0$, B^0B^0 or $\bar{B}^0\bar{B}^0$) created in the electron-positron annihilation.

In the *BaBar* experiment, the flavor of the tag B meson is determined by its daughter particles, and the event itself is evaluated based on a specific decay mode present. In Belle, an algorithm assigning a continuous dilution factor for a given event was used instead of discrete categorization of events. [3]

The probability of wrong tag determination is expressed by a wrong tag fraction w_{B^0/\bar{B}^0} for each of the tagging options or the average wrong tag probability w .

The rate of B_{sig} decaying into a flavor-specific state for events with tag B flavor being $B^0(+)$ respectively $\bar{B}^0(-)$ is, neglecting the Δw , is again given by [3] [2]:

$$f_{\pm}^{flv}(\Delta t) = \frac{\exp -\frac{|\Delta t|}{\tau_B}}{4\tau_B} \left\{ 1 \mp \Delta w \pm \mathcal{D} [S \sin \Delta m \Delta t + A \cos \Delta m \Delta t] \right\} \quad (2.11)$$

Events, for which $\lambda = 0$ (see relation (2.6)) corresponds to a flavor-specific eigenstate and are therefore used for mixing studies. The values of the coefficients in this case are $A = -1$ and $S = 0$. Studied events and $B^0\bar{B}^0$ systems can be classified according to whether the tag and signal meson are in with the same (SF) or opposite flavor (OF) states. The probability density function for the SF or OF event, as function of proper decay time difference Δt and the studied mixing frequency Δm_d , can be expressed by [3]:

$$f_{SF/OF}(\Delta t) = \frac{\exp -\frac{|\Delta t|}{\tau_B}}{4\tau_B} [1 \mp \Delta w \mp \mathcal{D} \cos \Delta m \Delta t] \quad (2.12)$$

In analogy with the asymmetry relation (2.9) the Δt -dependent asymmetry observable can be defined for SF and OF B -meson pairs [2]:

$$\mathcal{A}_{mixing}(\Delta t) = \frac{N_{SF}(\Delta t) - N_{OF}(\Delta t)}{N_{SF}(\Delta t) + N_{OF}(\Delta t)} \quad (2.13)$$

2.3 Proper Decay-Time Difference

The proper decay time difference is an essential component of time-dependent CP asymmetries, and crucial to successful measurement and understanding of the $\sin 2\phi_1$ and other angles of the Unitarity triangle [26]. Therefore, the motivation for its measurement comes both, from theory as well as experiment.

In the case of B-factories, the B mesons are created almost at rest with respect to the $\Upsilon(4S)$ center of mass system and fly out in a direction almost parallel to the z-axis. The asymmetric nature of the collisions in which these B mesons are produced provides the system with a non-zero boost in the laboratory frame (LAB). This creates a unique opportunity for measurement of decay time difference of the mesons, which are, thanks to the boost, given a chance to decay with some spatial separation observable in the LAB system. The decay-time of B mesons is determined using the decay length difference between the decay vertices of both neutral B mesons. When omitting the kinematic uncertainty caused by

neglecting the angle under which the daughter particle flies out with respect to the direction of the boost and the movement of B mesons in the rest frame of $\Upsilon(4S)$, the decay time difference can be defined as [3, 6]:

$$\Delta t = \frac{\Delta z}{(\gamma\beta)_{\Upsilon(4S)}c} \quad (2.14)$$

The Δz value represents the decay length difference between the decay vertices of both neutral B mesons along the z -axis and the $(\gamma\beta)_{\Upsilon(4S)}$ is the Lorentz boost of the $\Upsilon(4S)$ in the LAB system.

The physical distribution of the decay-time difference takes on the following form [3]:

$$f_{phys}(\Delta t) = \frac{1}{2\tau_B} \exp -\frac{|\Delta t|}{\tau_B} \quad (2.15)$$

The Belle experiment obtained the Δt values with the help of equation (2.14), whereas the *BaBar* experiment included the angle formed by the direction of the B meson flight and the z -axis into the variable calculation as can be seen in the Formula (2.18). However, none of these ways of calculation account for the small but non-zero boost of B -mesons in the $\Upsilon(4S)$ rest frame. Neglecting such factor introduces small bias on the Δz measurement, respectively the Δt calculation. This approximation is not considered by the Belle II `basf2` software either. Based on a consultation with the thesis supervisor, for the purpose of Monte Carlo data analysis introduced in further chapters of this work, a correction for this bias was incorporated manually by dividing each simulated Δt value by a $\gamma^* \approx 1.0019$ factor.

Experiment	Method	$\int \mathcal{L} dt$	
Neutral B meson lifetime		$[\text{fb}^{-1}]$	τ_{B^0} [ps]
<i>BaBar</i>	Incl. $D^*\ell\nu$	81	$1.504 \pm 0.030^{+0.018}_{-0.013}$
Belle	Excl. hadronic modes + $D^*\ell\nu$	140	$1.534 \pm 0.008 \pm 0.010$
Charged B meson lifetime			τ_{B^+} [ps]
<i>BaBar</i>	Excl. hadronic modes	21	$1.673 \pm 0.032 \pm 0.023$
Belle	Excl. hadronic modes	140	$1.635 \pm 0.011 \pm 0.011$

Table 2.1: τ_{B^0} and τ_{B^+} values measured by the BaBar and Belle experiments for selected final states [2] [27]

In the Table (2.3) you can find a comparison of the obtained values of B -meson lifetimes for selected final states along with luminosity available for the measurement. Lifetime fits were performed not only for the neutral B^0 , but also for charged B^+ mesons.

Figures (2.2) - (2.4) depict the results of Δt , CP asymmetry and flavor asymmetry (2.13) obtained by the Belle experiment using 140 fb^{-1} of recorded electron-positron collision data. Fitted values of CP parameters can be found in Table 2.3. These results were obtained using unbinned maximum likelihood fit of probability distributions described above.

The factor r appearing in Figure 2.3 originates in the tagging procedure employed in the Belle time-dependent CP asymmetry analysis. This so-called "dilution factor" r can take on values ranging from zero (corresponding to no flavor information; $\simeq w = 0.5$) to 1 (for clear flavor tag; $\simeq w = 0$) [3].

Experiment	$\int \mathcal{L} dt [fb^{-1}]$	
sin $2\phi_1$ parameter		
<i>BaBar</i>	29.7	$0.59 \pm 0.14 \pm 0.05$
Belle	140	$0.728 \pm 0.056 \pm 0.023$
Mixing frequency		
<i>BaBar</i>	29.7	$0.516 \pm 0.016 \pm 0.010$
Belle	140	$0.511 \pm 0.005 \pm 0.006$
Direct CP parameter λ		
<i>BaBar</i>	29.7	$0.93 \pm 0.009 \pm 0.02$
Belle	140	$1.007 \pm 0.041 \pm 0.033$

Table 2.2: Time-dependent CP parameter values measured by the BaBar and Belle experiments [2] [27]

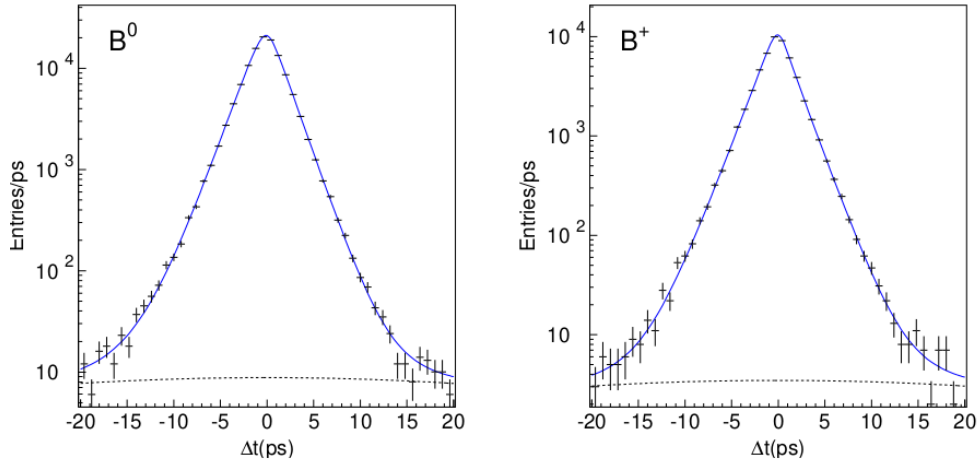


Figure 2.2: Δt fits performed by the Belle collaboration for B^0 and B^+ mesons [27]

2.4 Time resolution function

Resolution of the Δt variable is, among other factors, significantly affected by the precision of Δz measurement. Time-dependent studies of CP violation, B -lifetime, and $B^0\bar{B}^0$ mixing frequency have to account for a limited efficiency of the detector, tracking, and reconstruction precision of the software. This is done by a convolution of the resolution function $\mathcal{R}(\Delta t, \sigma_{\Delta t})$ describing imperfections of the variable determination with a probability distribution function (*p.d.f.*) of the variable's physical time-dependence $f_{phys}(\Delta t)$. In the case of simple proper decay time difference studies described in the following Chapter 3, the time evolution distribution takes on the form described by Formula (2.15). The observed time-dependent spectra follow [3]:

$$\begin{aligned}
 \mathcal{F} &= \int_{-\infty}^{\infty} f_{phys}(\Delta t_{true}) \mathcal{R}(\Delta t_{res}, \sigma_{\Delta t}) d\Delta t_{true} \\
 &= f_{phys}(\Delta t) \otimes \mathcal{R}(\Delta t_{res}, \sigma_{\Delta t})
 \end{aligned}
 \tag{2.16}$$

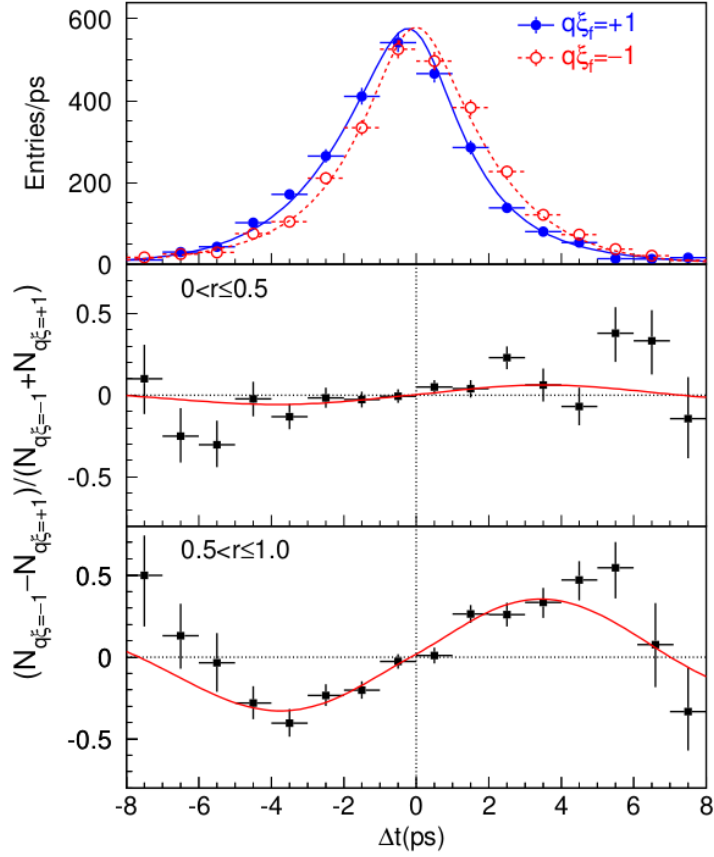


Figure 2.3: Belle Δt fit for both $\eta_{CP} \equiv q\xi_f = \pm 1$ final states and CP asymmetry measurement for $0 < r \leq 0.5$ and $0.5 < r \leq 1$ [27]

where $\sigma_{\Delta t}$ is the uncertainty of the measured value of Δt and Δt_{true} represents a real physical value unbiased by the detector response. The interpretation of the Δt_{res} variable can be twofold, depending on the kind of event samples analyzed:

$$\Delta t_{res} = \begin{cases} \Delta t - \Delta t_{true} & \text{if working with detector-collected datasets} \\ \Delta t - \Delta t_{MC} & \text{if working with MC samples} \end{cases} \quad (2.17)$$

where Δt_{MC} denotes a gen-level variable; Δt_{true} again the truth value of the B decay time difference; Δt denotes det-level variable. For the purpose of this work, the latter one applies. The nomenclature was adopted from the analysis software and is consistent with the variable names used for the analysis presented in further chapters.

The resolution function used by the *BaBar* experiment was formed by a sum of three Gaussian kernels describing the core, tail and outlier parts of the spectra. The characteristics of the *BaBar* resolution function depend on parameters obtained from Monte Carlo simulations and analysis of B meson decay samples. These parameters vary for each of the different event flavor tags [2, 3].

In order to improve the precision of the Δz measurement in case of events with fully reconstructed B_{sig} vertex, the kinematic approximation which assumes zero momentum of B -mesons in the center of mass frame was partially corrected

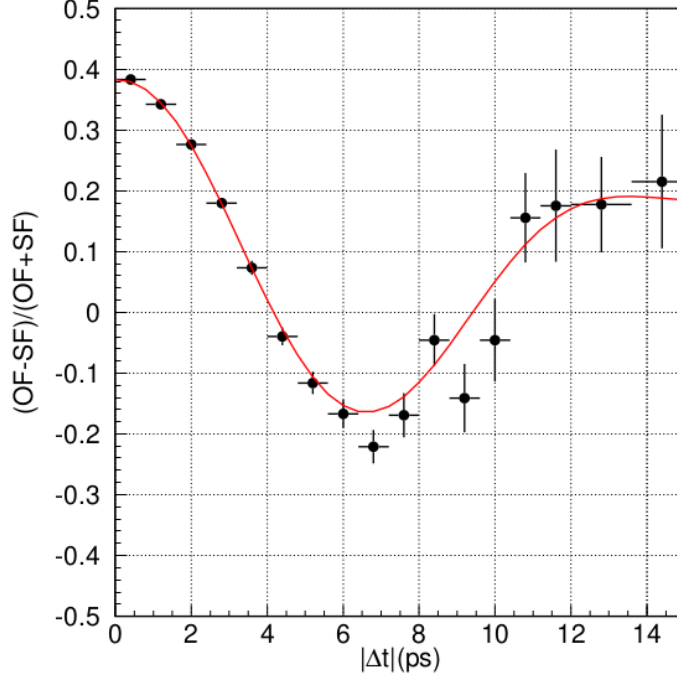


Figure 2.4: Time-dependent flavor asymmetry unbinned maximum likelihood fit from Belle measurement [27]

for in the following way [2]:

$$\Delta z = \beta\gamma\gamma_{rec}^*c\Delta t + \gamma\beta_{rec}^*\gamma_{rec}^*\cos\theta_{rec}^*c(\tau_B + |\Delta t|) \quad (2.18)$$

where the variables labeled with an asterisk refer to B_{sig} in the center of mass frame with the angle being associated with the direction of particle momentum w.r.t. the boost direction in the center-of-mass frame.

At BaBar the full time resolution function took on a general form [2]:

$$\begin{aligned} \mathcal{R}^{BaBar}(\Delta t_{res}, \sigma_{\Delta t}) = & f_{core}G_{core}(\Delta t_{res}, \mu_{core}\sigma_{\Delta t}, s_{core}\sigma_{\Delta t}) + \\ & f_{tail}G_{tail}(\Delta t_{res}, \mu_{tail}\sigma_{\Delta t}, s_{tail}\sigma_{\Delta t}) + \\ & f_{outlier}G_{core}(\Delta t_{res}, \mu_{outlier}\sigma_{\Delta t}, s_{outlier}\sigma_{\Delta t}) \end{aligned} \quad (2.19)$$

On the other hand, the Belle I resolution function [12] is (under the assumption of all contributing phenomena being statistically independent) constructed as a convolution of several components. It consists of four terms which incorporate the effects of vertex resolution for both, the B_{tag} as well as the B_{sig} decay vertex reconstruction which are described by a double-Gaussian (R_{det}^{sig} and R_{det}^{tag}), the impact of a non-primary vertex components R_{NP} causing smearing of the z -coordinate measurement of B_{tag} due to tracks originating from charm particle decays in flight and kinematic approximation (R_{kin}) of B mesons being produced at rest in the $\Upsilon(4S)$ rest frame. The second to last component is described by a delta and an exponential function. The kinematic term (R_{Kin}) takes into account the angle formed by the B meson momentum and the direction of boost as well as the meson's momentum and energy in the same frame [3, 28].

$$\mathcal{R}^{Belle}(\Delta t_{res}, \sigma_{\Delta t}) = R_{det}^{sig} \otimes R_{det}^{tag} \otimes R_{NP} \otimes R_{kin} \quad (2.20)$$

The resolution of the detector is accountable for significant smearing of the final resolution spectra, while the errors in flavor tagging dilute the asymmetry between events of different B_{tag} flavor [2, 12].

3. MC/Data validation of vertex tagging constraints

3.1 GRID and remote data processing

The Belle II experiment is expected to need a large amount of computing power and storage. Distributed computing system ("GRID") [29, 30] is inevitable for performing demanding calculations and handling sizeable data quantities. The Belle II grid connects many distributed computing resources from all over the world (including the Czech Republic). The Belle II data taking can be generally divided into sections called experiments. These last several months during which all parts of the Belle II detector record data from collisions. These data are further collected in a raw form by the Belle DAQ system [29].

Before the physical analysis of collected data begins, detector calibration constants have to be determined. These constants contain information about the condition of the detector, the state of the accelerator as well as the current status of detector alignment. Their values are important as an input for raw data processing as well as Monte Carlo simulation.

The mini data summary tables (mDST) [29] are the result of data processing and contain information about particle type and physical properties. The mDSTs are copied onto GRID sites, where the physics analysis is carried out. Selected event candidates for a particular process or decay channel from the mDSTs are saved into a unique analysis-connected format called nTuple. This format stores information about particle properties, kinematic characteristics of the event and can be directly downloaded to a personal site. The nTuple production is when a grid basf2 (gbasf2) [30], distributed computing interface of the Belle II analysis software framework, comes to play. Using a steering file, python based scripts, and a command line, the user can easily remotely submit and manage jobs on the GRID site and access stored MC and data files.

3.2 BeamSpot Calibration

The aim of the BeamSpot calibration is to determine the probability distribution function of the primary interaction vertices, i.e., properties of the luminous region of the collisions. The knowledge of the BeamSpot properties is crucial in the time-dependent CP violation analyses as well as, for example, for the D -meson lifetime measurement [28, 31].

The BeamSpot parameters are calibrated using $ee \rightarrow \mu\mu$ events. Recently, an improved algorithm to determine these parameters was developed by the thesis supervisor.

The older, vertexing-based version of the BeamSpot calibration algorithm was, to a great extent, affected by the tracking precision and provided an inaccurately large size of the region, especially along the y -axis. It also neglected changes in the position of the BeamSpot within a single run. These are observable at the scope of tens of minutes, while the calibration was only performed once per run,

which can last up to 8 hours [28].

A new time-dependent calibration tool was therefore developed. It minimizes the effect of tracking resolution and incorporates run segmentation to account for the IP movement.

3.3 Tag-side Vertexing Constraints

The vertex reconstruction quality has a significant impact on the precision of time-dependent CP violation effects studies. It affects them through the calculation of spatial separation of B -meson decay vertices which transfers to the proper decay-time measurement. In order to improve the quality of the B -meson vertex position determination, various constraints can be imposed.

Signal and tag B vertices are fitted individually. Reconstruction of the less accurate tag B vertex can be performed using three different constraint options - "noConstraint", "IP" and "Tube". The signal B meson vertex, reconstructed using `treeFitter` [32, 33] has only two options: a "noConstraint" fit or "IP-pointing" constraint. Applying either of the "IP" and "Tube" for the tag-side vertexing automatically includes the "IP-pointing" constraint for the signal side of the event.

At Belle and *BaBar*, a simple "IP" constraint based on the BeamSpot position (illustrated in Figure 3.1) sufficed. This constraint focuses the fitting procedure into the luminous region within close proximity of the interaction point (hence the name "IP-constrained" fit). The "IP"-constraining gave a good quality fit since both B -meson decay vertices were localized inside the BeamSpot region. However, due to a different beam scheme and two times better tracking precision at Belle II, a more sophisticated constraining method was necessary. A considerably smaller BeamSpot size ($6 \times 0.06 \times 150 \mu\text{m}^3$) [34] means the B -mesons decay out of the luminous region, which diminishes the quality of vertex fit.

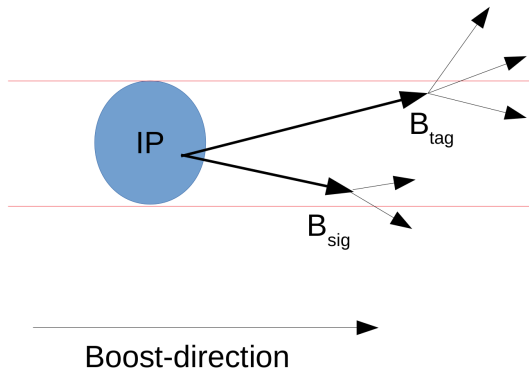


Figure 3.1: "IP" constraint for B_{tag} vertexing

Consequently, a new constraint, known as the "Tube" constraint illustrated in the Figure 3.2, was added to the reconstruction software. Using this constraint, first, one B -meson decay vertex is fully reconstructed (B_{sig}). Its track is subsequently extrapolated to the BeamSpot region, and the vertex fitting procedure is applied.

This way the position of the primary interaction point is obtained. Using the four-momentum and energy conservation, a tube-like element is extended in the estimated flight direction of the other B-meson. The fit of the B_{tag} vertex is then narrowed down to the area defined by the tube [34]. The "Tube" constraint partially mitigates worse resolution of the tag side vertex fit, caused by missing neutrino energy and tracks originating from a non-primary vertex (for example, from D meson decays).

The purpose of the validation studies, which is presented in the next section, is to find the combination of the mentioned options that lead to the most precise analysis results.

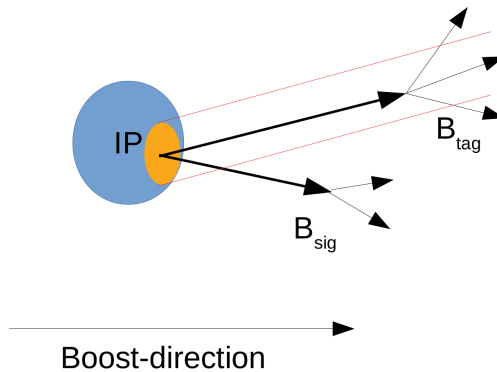


Figure 3.2: "Tube" constraint for B_{tag} vertexing

3.4 Validation - MC/Data comparison

3.4.1 MC and Data Samples

The performance of each constraint was checked in Summer 2020 by a MC/Data comparison analysis. The Monte Carlo dataset from the thirteen Belle II official runs in an independent campaign (MC13a) was used for the Summer 2020 simulation studies. It was processed using an older `basf2` software release 4 available at the time of the study.

This data collected throughout the year 2019 corresponds to experiments 7, 8 and 10 and sums up to $\sim 8.7 \text{ fb}^{-1}$ of the integrated luminosity. This dataset was used for the first round of the Monte Carlo and Data comparative studies with a focus on the tag-vertexing constraint validation.

The experience gained from the analysis performed on the 2019 data prompted a revisit once a new time-dependent algorithm for BeamSpot calibration became available for validation. A fraction of the data sample from Experiment 12 collected in spring 2020 period was processed for this purpose. Approximately $\sim 20 \text{ fb}^{-1}$ were processed for validation of three different tag-vertex constraints "noConstraint", "IP" and "Tube" constraint utilizing this new calibration. Results of these follow-up studies are presented in the latter half of this chapter.

The processing was performed using adjusted variations of existing scripts prepared for the spring 2020 data processing. The procedure consisted of two

steps. First, the mDST files from GRID were pre-selected for particular needs and characteristics of each of the nine studied channels to prepare ROOT nTuples. Second, the obtained nTuples were subject to further background suppression and quality selection. The background reduction was performed using boosted decision tree (BDT) method [32, 35] by scripts inherited from the first analysis series.

Cuts applied to the data correspond to the ones used for spring 2020 processing. Their list and description can be found in [36]. The data were again processed by an (with respect to the currently available one) older basf2 software release 4.

This procedure was performed for nine different decay channels, namely:

- $B^0 \rightarrow D^-(\rightarrow K^+\pi^-\pi^-)\pi^+$
- $B^0 \rightarrow D^{*-}(\rightarrow [\bar{D}^0 \rightarrow K^-\pi^+]\pi^-)\pi^+$
- $B^0 \rightarrow D^{*-}(\rightarrow [\bar{D}^0 \rightarrow K^-\pi^+\pi^-\pi^+]\pi^-)\pi^+$
- $B^0 \rightarrow [J/\Psi \rightarrow \mu^+\mu^-][K_S^0 \rightarrow \pi^+\pi^-]$
- $B^0 \rightarrow [J/\Psi \rightarrow e^+e^-][K_S^0 \rightarrow \pi^+\pi^-]$
- $B^+ \rightarrow [J/\Psi \rightarrow \mu^+\mu^-]K^+$
- $B^+ \rightarrow [J/\Psi \rightarrow e^+e^-]K^+$
- $B^+ \rightarrow [\bar{D}^0 \rightarrow K^-\pi^+]\pi^+$
- $B^+ \rightarrow [\bar{D}^0 \rightarrow K^-\pi^+\pi^-\pi^+]\pi^+$

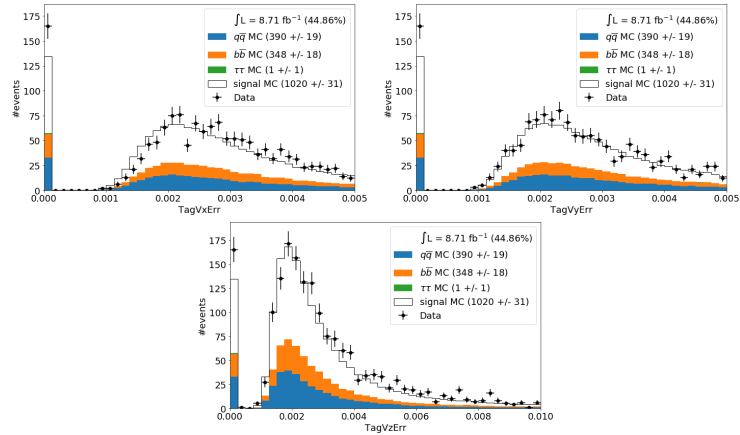
The results are demonstrated on the $B^0 \rightarrow D^-(\rightarrow K^+\pi^-\pi^-)\pi^+$ mode analysis.

3.4.2 Summer 2020 Monte Carlo and Data Tag-side Vertexing Constraint Validation

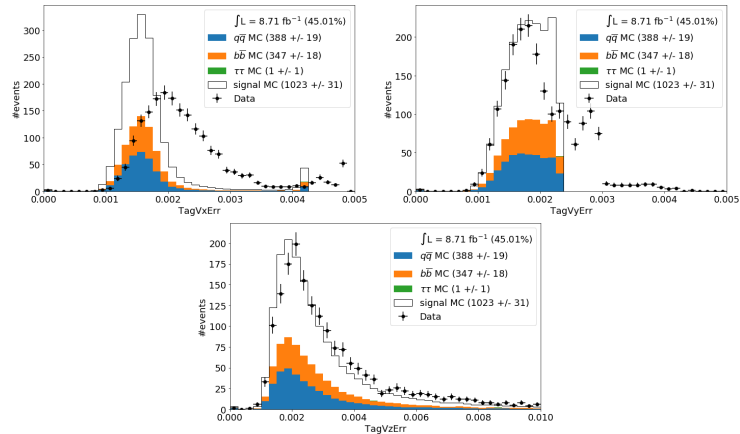
The Figure 3.3 compares the MC and data analysis results obtained in Summer 2020. All three possibilities of B_{tag} decay vertex reconstruction were validated and results were compared. The depicted variables represent the Tag vertex position uncertainty in each coordinate. The first row corresponds to results obtained with the "noConstraint" option, the other two lines show results for the "IP" and "Tube" vertexing constraints, respectively.

Figure 3.3 demonstrates the inconsistency between the MC and data for the "Tube" and "IP" predominantly in the x and y coordinate. The data and MC distribution shapes for the tag-side vertex position uncertainties did not agree for either of the more complex validated constraint options and deviated especially in the case of the "IP" constraint. This effect highlights the imperfection of the description of the luminous region. The MC sample was simulated with a much larger BeamSpot size in the y -direction than really is in data. As the reconstruction precision in the z direction is higher, the discrepancies are not as pronounced.

Vertexing of tagging side with "noConstraint" option: Nice agreement



Vertexing of tagging side with "IP" option: Systematic disagreement



Vertexing of tagging side with "Tube" option: Small systematic disagreement

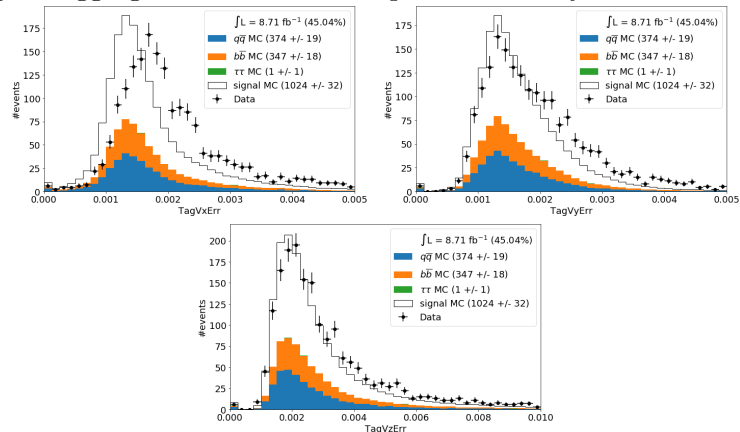


Figure 3.3: MC and data comparison - Summer 2020: tag-side vertexing option validation results. The depicted variables represent Tag B vertex position uncertainty in the corresponding coordinate. The units for the variables on the horizontal axes are [cm]

Thanks to the results of the Summer 2020 comparative analysis, the issues with the BeamSpot information became more apparent. That prompted the development of the aforementioned new calibration algorithm able to suppress the tracking effects and evade the limitation of the imprecise vertexing output. Based on the results, the prompt analysis performed by the TDCPV group [36] did not use any of the mentioned constraints, and the "noConstraint" option was opted for instead.

3.4.3 Fall 2020 Monte Carlo and Data Comparison - Tag-side Vertexing Constraint and BeamSpot Calibration Validation

As the new beam-constraining time-dependent calibration described in Section 3.2 was included in the software, we could check whether this solves the problem observed in Summer 2020 studies. First, for comparison, the variables describing the uncertainty on the B_{tag} meson decay vertex position are displayed in Figure 3.4. The organization of the results follows the same line -in addition to the "noConstraint" option for both event sides depicted in the first row, the "IP" and "Tube" constraint on the tag-side including the "IP-pointing" constraint option for the signal side can be found in the second and third row, correspondingly.

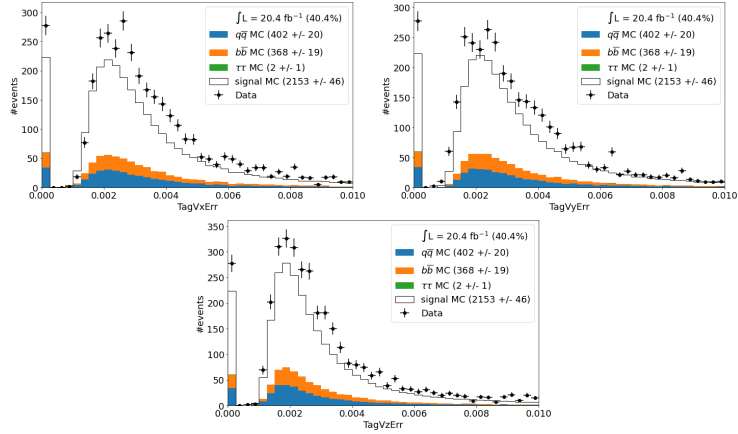
As can be seen from the comparison of the validation with and without the new calibration constant applied, the results for processed data visibly improved after its addition. The plots in the first row, corresponding to the "noConstraint" option, show good agreement between the MC simulation and reconstructed data. The observed shapes of the spectra agree and are aligned. This was, however, also the case for the Summer 2020 studies.

More significant changes can be observed for dependencies in the second and third figure segment. A new trend appears - the distributions corresponding to data are shifted towards the origin of the graph, in particular for the x and y -coordinates. Predominantly in the case of the TagVyErr variable for the "IP" constraint, we observe a large discrepancy between the MC and Data spectrum shape. For the uncertainty on the z -component variable, the deviation and the shift towards zero is less pronounced. The general trends for the MC and data for this variable agree. This might indicate that the uncertainties and errors in the vertex position, which are obtained from data using the new calibration setting, are smaller than the ones we get from the MC datasets. The MC was processed in spring 2020 without this new calibration, unlike the data it is being compared with. The inaccurately large size of the luminous region, particularly in the y -direction, should be cured within the new MC14.

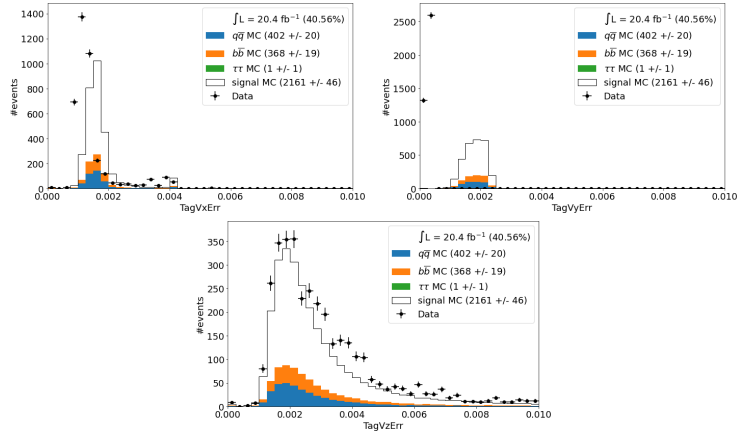
For the "Tube" option applied to the vertexing procedure, the discrepancy in the general shape of the spectra does not reappear when looking at the TagVyError graph. As can be seen, the remaining two variables (associated with x and z coordinates) manifest a similar trend as for the "IP" constraint option. The overall shapes of the dependencies agree, and, with respect to the Monte Carlo shapes, we observe a significant shift of the data spectra towards the zero value. This shift suggests the BeamSpot calibration, only applied to the newly processed data, has a positive effect on the reconstruction.

Taking a look at variables associated with the signal side showed in Figure 3.5,

Vertexing of tagging side with "noConstraint" option:



Vertexing of tagging side with "IP" option:



Vertexing of tagging side with "Tube" option:

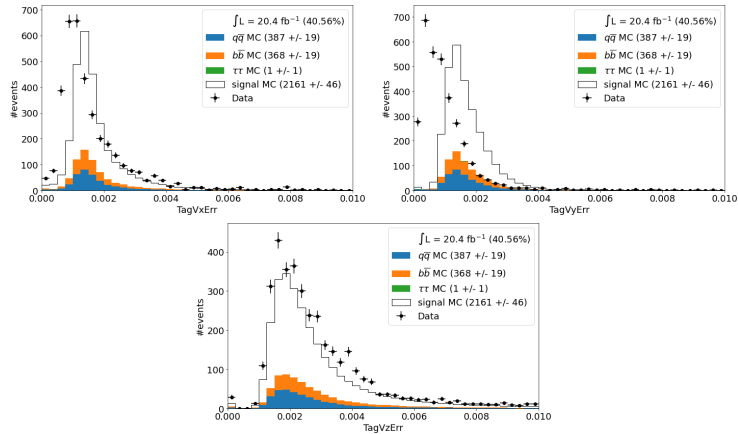
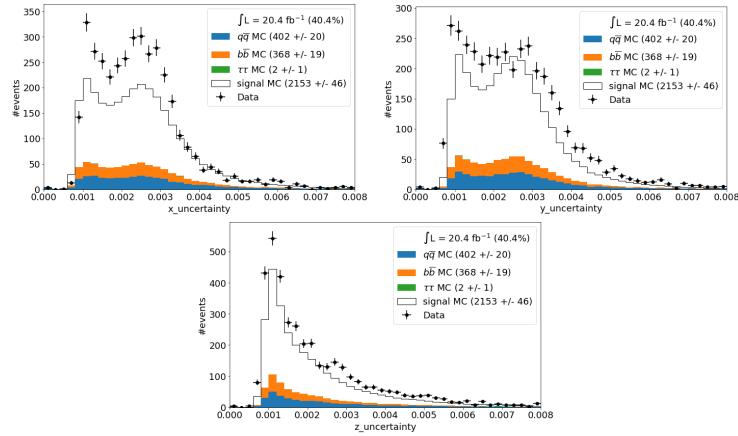


Figure 3.4: MC and data comparison - Fall 2020 tag-side vertexing option validation results. The meaning of the depicted variables is the same as in Figure 3.3. The units for the variables on the horizontal axes are [cm].

the uncertainties of the IP position coordinates show satisfactory agreement for the "noConstraint" option. In the case of the "IP-pointing" constraint, not only a general disagreement in shape is observed, but the aforementioned shift towards the origin of the graph is also present. This observation suggests the

Vertexing of the signal side with the "noConstraint" option:



Vertexing of the signal side with the "IP - pointing constraint":

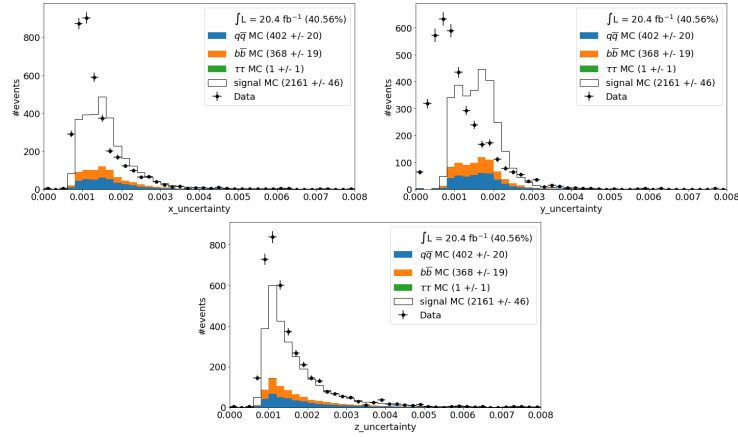


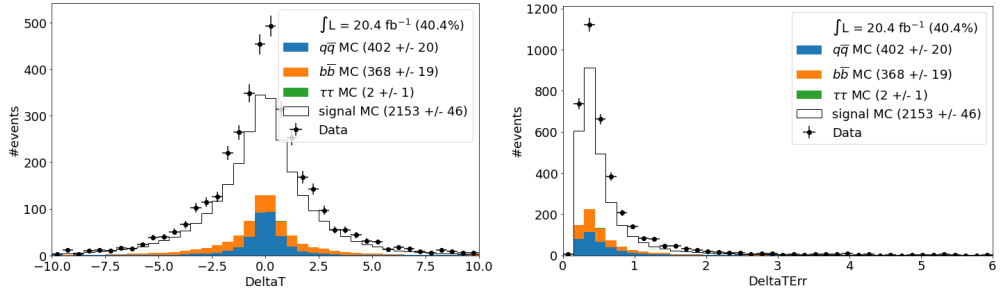
Figure 3.5: MC and data comparison - signal side validation results. The depicted variables represent the signal B vertex position uncertainty in the corresponding coordinate. The units for the variables on the horizontal axes are [cm].

above-mentioned patterns are not associated only with the B_{tag} vertex reconstruction. It can be seen that the signal side constraint squeezes the uncertainty for data to zero. The tag-side constraint does not affect the curves shown in this plot. The reason behind this most probably lies again in the MC13, which was generated with a large size of the luminous region. This is true especially for the y coordinate as it was generated with a size of $13 \mu\text{m}$, whereas the real size in data is less than $1 \mu\text{m}$. The overall change is considered positive, as judging by the results for data analysis, the newly applied BeamSpot calibration seems to significantly improve the uncertainties on the reconstructed vertex position.

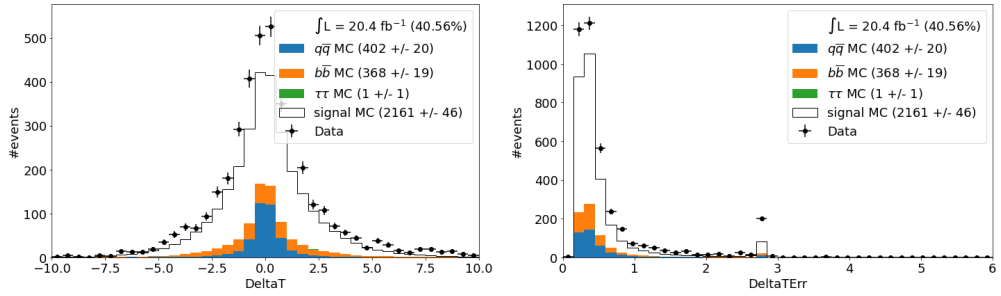
In Figure 3.6 we see the impact of constraining on the proper decay-time difference for the two B mesons (first columns) and the estimate of the uncertainty of this variable (the second column). The IP and Tube constraint show minor improvement in the Δt measurement resolution. In addition, the "Tube" constraint appears to be able to eliminate the little peak in Δt_{Err} observed for the "IP" constraining option.

Figure 3.6 emphasizes the fact that the Δt variable is reconstructed (in terms of the kinematic approximation) utilizing the measurement of the Δz spatial

Vertexing of tagging side with "noConstraint" option:



Vertexing of tagging side with "IP" option:



Vertexing of tagging side with "Tube" option:

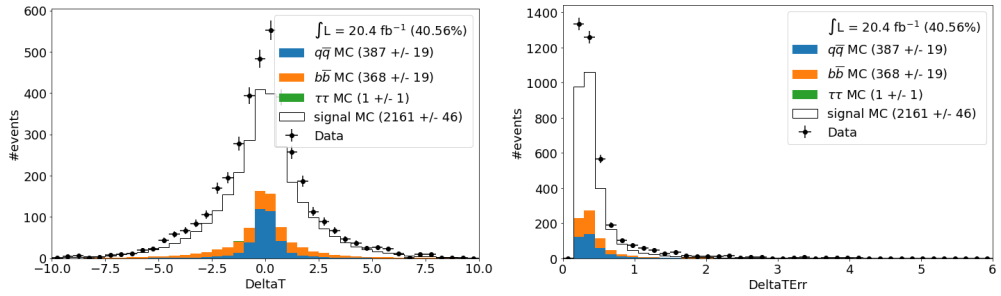


Figure 3.6: MC and data comparison - tag and signal decay time residual. The units for the variables on the horizontal axes are [ps].

separation of decay vertices. As it could be seen from the previous plots, the variables associated with the z -coordinate are least affected by the tag-side vertexing procedure.

Thanks to the reconstruction precision being the highest for this coordinate, the vertexing constraints and BeamSpot issues in the older versions of reconstruction software do not significantly impede the determination of Δt . The uncertainty on the proper decay time difference slightly improves. However, not applying the vertexing constraints does not seem to impair the measurement too dramatically.

To achieve better agreement between data and MC distributions, the MC has to be generated with the same conditions of the luminous region as there are in data. At the time of processing the MC13 data sample, that was not possible since the BeamSpot size in the data was not yet correctly determined. This incorrect value was used in the MC13 production. This cannot be corrected afterward, and the only option is a new MC campaign. In the new MC14 campaign, the MC beam conditions should be much closer to the real conditions in data (as they are

now known better from the new BeamSpot algorithm).

4. Resolution Function Studies

4.1 Belle II Resolution Function

To accurately model the effects of reconstruction, background, and detector resolution on the measured values of the Δz variable essential for the decay-time difference determination, the physical distribution corresponding to the variable of interest is, in general, convoluted with a so-called resolution function. This gives one a probability distribution function. The Time-Dependent CP Violation working group is currently, among other types of analysis, working on the development of an improved, more precise time resolution function. Parallel efforts are made by the group studying the semi-leptonic decay channels as well as by the groups analyzing the hadronic modes.

The approach of the semi-leptonic group is to a great level inspired by the approach adopted in Belle I analysis [12]. In contrast, many physicists are currently working on developing a new resolution model well suited for Belle II, where, due to the much higher expected statistics, the systematic effects have to be under control.

Taking advantage of the hadronic channel characteristics, this function should be universal for all available channels. Sophisticated studies are being performed to find the optimal balance between simplicity and efficiency, starting with a simple double-Gaussian kernel subsequently augmented by two exponential tails.

As was demonstrated in the Summer 2020 study published in [36], the final form of the resolution function needs to incorporate a correlation between the time resolution function and lifetime fits and errors on the studied Δt variable.

While waiting for the final form of the resolution function, some complementary studies can be performed in order to test various aspects and characteristics of simpler resolution function models with common features. In the remaining part of this thesis, an example of such studies is introduced, and results obtained over the course of the past few months are presented.

Two differently processed and reconstructed collections of MC were analyzed, and attributes of the obtained results were compared.

4.2 Technical Details

4.2.1 Variables and Important Relations

As is mentioned in the Section 2.3, thanks to the boost of the $B\bar{B}$ -pair, it is possible to study the proper decay-time difference of such a system and use this information to probe the CP violation in the B meson sector.

Several different decay-time-related variables were used throughout the analysis and will be mentioned in the further parts of this chapter. Namely, these MC-sample related variables are:

- $\text{MCDeltaT}(\Delta t_{MC})$ - A generator-level (\equiv does not account for detector effects) equivalent of the DeltaT variable. MCDeltaT values correspond to a generated value of proper decay time difference in [ps] affected by the

Δz kinematic approximation. Its values are calculated using the following formula:

$$\Delta t_{MC} (\equiv \text{MC}\Delta t) := \frac{z_{\text{sig}}^{\text{MC}} - z_{\text{tag}}^{\text{MC}}}{(\gamma\beta)_{\Upsilon(4S)}c} \quad (4.1)$$

for $\beta\gamma$ representing boost factor of the $\Upsilon(4S)$ particle in the laboratory system. This variable is accessible only in MC.

- **DeltaT** (Δt) - proper decay time difference between the signal B -meson decay time t_{sig} and the tagged B meson decay time t_{tag} in the Δz kinematic approximation (in [ps]). It is a detector-level variable which also accounts for the resolution effects of the detector measurement. Δt values are calculated by the means of the following formula

$$\begin{aligned} \Delta t (\equiv \text{DeltaT}) &:= t_{B_{\text{sig}}}^{\text{approx}} - t_{B_{\text{tag}}}^{\text{approx}} \\ &= \frac{z_{\text{sig}} - z_{\text{tag}}}{(\gamma\beta)_{\Upsilon(4S)}c} \end{aligned} \quad (4.2)$$

This variable can be found in data as well as in MC simulated samples.

- **DeltaT Residual** (referred to also as Δt_{res}) - represents a difference between the **DeltaT** and **MCDeltaT** variables for the purpose of resolution function studies.

$$\begin{aligned} \Delta t_{\text{res}} &:= \Delta t - \Delta t_{MC} \\ &(\equiv \text{DeltaT} - \text{MC}\Delta t) \end{aligned} \quad (4.3)$$

However, as mentioned previously in the ref{chap tdcpv} the **basf2** software does not account for the non-zero boost of B -mesons in the $\Upsilon(4S)$ rest frame for none of these variables. This effect is corrected by dividing each value by a $\gamma^* \approx 1.0019$ factor. Hereafter, the notation of the variables does not change, but the additional $\frac{1}{\gamma^*}$ factor multiplication is assumed.

4.2.2 Older MC Sample

The same signal MC samples as in the case of MC/Data comparative studies introduced in the previous chapter were used for the resolution function studies. For overall 9 hadronic decay channels, Table 4.4, a total of 500 000 - 2 000 000 $B\bar{B}$ events per channel (depending on a decay mode) were reconstructed using the thirteen Belle II run-independent campaign MC13a processed using an older **basf2** version 4 available in Summer 2020. The generated MC value of a neutral and charged B -meson lifetime for the release 4 corresponds to:

$$\begin{aligned} - \tau_{MC}(B^0) &= 1.525 \text{ ps} \\ - \tau_{MC}(B^\pm) &= 1.638 \text{ ps} \end{aligned}$$

The signal B -meson decay vertex was fitted using **TreeFitter** [33] with no pointing constraint, whereas vertexing of the tag side of the event was performed with **Rave** fitter [37]. No tag vertex constraint was applied as a result of ongoing BeamSpot issues at that time (see Chapter 3 on MC/data Comparison).

Decay channel	Channel Label
$B^0 \rightarrow D^-(\rightarrow K^+\pi^-\pi^-)\pi^+$	B0toPiDPtoK2Pi
$B^0 \rightarrow D^{*-}(\rightarrow [\bar{D}^0 \rightarrow K^-\pi^+]\pi^-)\pi^+$	B0toPiDStoK2Pi
$B^0 \rightarrow D^{*-}(\rightarrow [\bar{D}^0 \rightarrow K^-\pi^+\pi^-\pi^+]\pi^-)\pi^+$	B0toPiDStoK4Pi
$B^0 \rightarrow [J/\Psi \rightarrow \mu^+\mu^-][K_S^0 \rightarrow \pi^+\pi^-]$	B0toJPsiKStoMuMu
$B^0 \rightarrow [J/\Psi \rightarrow e^+e^-][K_S^0 \rightarrow \pi^+\pi^-]$	B0toJPsiKStoEE
$B^+ \rightarrow [J/\Psi \rightarrow \mu^+\mu^-]K^+$	BPtoJPsiKtoMuMu
$B^+ \rightarrow [J/\Psi \rightarrow e^+e^-]K^+$	BPtoJPsiKtoEE
$B^+ \rightarrow [\bar{D}^0 \rightarrow K^-\pi^+]\pi^+$	BPtoPiD0toKPi
$B^+ \rightarrow [\bar{D}^0 \rightarrow K^-\pi^+\pi^-\pi^+]\pi^+$	BPtoPiD0toK3Pi

Table 4.1: B decay modes used for the analysis

Following nine channels, five corresponding to neutral B^0 decay channels and four to charged B^+ the modes¹, were further used for resolution and lifetime fits:

The table contains alternative labels of the channels used hereafter throughout the thesis.

4.2.3 New MC Dataset

The second data collection corresponds to 5 ab⁻¹ MC dataset processed with a newer release 5 of the `basf2` software available in winter 2020. Using this newer release, only three channels were reconstructed in this processing, namely:

- $B^0 \rightarrow D^-(\rightarrow K^+\pi^-\pi^-)\pi^+$
- $B^0 \rightarrow D^{*-}(\rightarrow [\bar{D}^0 \rightarrow K^-\pi^+]\pi^-)\pi^+$
- $B^0 \rightarrow D^{*-}(\rightarrow [\bar{D}^0 \rightarrow K^-\pi^+\pi^-\pi^+]\pi^-)\pi^+$

The signal B meson decay vertex was reconstructed using `TreeFitter` [33] with IP pointing constraint. `Rave` [37] was used for the tag B vertex reconstruction again. However, this time the "Tube" constraint was applied (see the following section

4.2.4 Kinematic Approximation

Different approaches were adopted when incorporating the effects of kinematic smearing into analysis. As already mentioned, the Δt variable is not measured directly, but rather approximately calculated as a difference of the z coordinates² corresponding to B meson decay vertices. The kinematic smearing can be included by adding a second, correction term, to the original expression:

$$\Delta t = \frac{\Delta z}{c\beta\gamma\gamma^*} + \frac{\beta^*}{\beta} \cos\theta \sum t \quad (4.4)$$

where $\gamma\beta$ describes boost of the $\Upsilon(4S)$ w.r.t. the laboratory frame, β^* denotes velocity of the B meson in the $\Upsilon(4S)$ center of mass frame (CMS) and γ^* takes

¹For the decays of the charged B , also the charge conjugated modes are included.

²I.e. in direction parallel with the $\Upsilon(4S)$ momentum, in the so-called boost direction

resolution function described above. Values of 11 free-floating parameters are obtained by an iterative application of the minimizing algorithm.

B Second step - DeltaT variable fit and B lifetime determination

The subsequent step utilizes the prior obtained parameter values. These are fixed for the `DeltaT` fit and the distribution is fitted by a convolution of the resolution function \mathcal{R} (with fixed parameter values) and physical distribution $f_{phys} = \frac{1}{2\tau_B} \exp -\frac{|\Delta t|}{\tau_B}$ as described by Formula (2.16). In addition, the kinematic smearing is added to the convolution. The only free parameter of this fit is the τ_B .

C Additional steps

At first, the procedure was performed with very few quality requirements imposed on the data (see Section (4.3.2)). Results of this preliminary studies can be found in Table 4.2 and Table 4.3. In order to check the validity of the results and the ability to obtain correct values of B -meson lifetime using the described form of resolution function, the procedure was tested on the `MCDeltaT` variable spectrum. As the generator-level MC-truth variable is not affected by detector resolution physical distribution with the kinematic smearing was used for the fit. The goal was to refute the possibility of the resolution function causing discrepancies in the fitted lifetime values and those used for MC generation. Further control analysis was performed on a dataset processed with a newer version 5 of the `basf2` software with the purpose of monitoring the effect of a software release version, Tube constraint, and time-dependent beam-spot calibration algorithm application. Additional quality cuts were imposed on the data. The results of this more restrictive analysis are described in detail for each of the analyzed chapters in the following subsections. The same analysis was performed with the control sample processed by the recent software release 5.

4.3 Results

4.3.1 MC processed before Summer 2020

4.3.2 Preliminary Studies

As a very step, a quick resolution function study was performed. Signal MC samples simulated before Summer 2020 were used, and with respect to the quality of data, two cuts were used:

- `isSignal = 1`
- `TagVpVal > 0.01`

The first cut imposed on the variable `isSignal` selects particles recognized as correctly reconstructed whereas the cut on the `TagVpVal` removes events very low or zero value of the B_{tag} -decay vertex momentum. The tag side vertices for which the fitting procedure fails are by default assigned value `TagVpVal = 0`. The purpose of this study was to verify that this form of function is able to fit

the decay time residual distributions. It also provided an estimate of the precision achievable when working with data of varying quality. The numerical results of the lifetime fitting procedure are listed in Table 4.2.

Channel	τ_B [ps]	$\frac{\tau_B - \tau_B^{MC}}{\sigma_{\tau_B}}$
B0toJPsiKStoEE	1.492 ± 0.004	-8.3
B0toJPsiKStoMuMu	1.502 ± 0.003	-7.7
B0toPiDPtoK2Pi	1.505 ± 0.003	-6.7
B0toPiDStoK2Pi	1.479 ± 0.005	-9.2
B0toPiDStoK4Pi	1.246 ± 0.005	-55.8
BPtoJPsiKtoEE	1.635 ± 0.004	-0.8
BPtoJPsiKtoMuMu	1.641 ± 0.003	1.0
BPtoPiD0toK3Pi	1.558 ± 0.003	-26.7
BPtoPiD0toKPi	1.630 ± 0.002	-4.0

Table 4.2: B -meson τ values from a preliminary `DeltaT` fit

Since the results deviated from expected values by high multiples of statistical uncertainty, the fitting procedure was repeated on a `MCDeltaT` variable. Since the lifetime value used for MC generation was checked prior to this analysis, this step helped clarify whether the function is causing the observed discrepancy. Results are to be found in Table 4.3.

Channel	τ_B [ps]	$\frac{\tau - \tau_{MC}}{\sigma_{\tau}}$
B0toJPsiKStoEE	1.546 ± 0.003	7.0
B0toJPsiKStoMuMu	1.547 ± 0.002	11.0
B0toPiDPtoK2Pi	1.549 ± 0.002	12.0
B0toPiDStoK2Pi	1.562 ± 0.003	12.3
B0toPiDStoK4Pi	1.694 ± 0.004	42.3
BPtoJPsiKtoEE	1.641 ± 0.003	1.0
BPtoJPsiKtoMuMu	1.645 ± 0.002	3.5
BPtoPiD0toKPi	1.645 ± 0.002	3.5
BPtoPiD0toK3Pi	1.679 ± 0.003	13.7

Table 4.3: B -meson τ values from a preliminary `MCDeltaT` fit

4.4 Time Resolution Function and Lifetime Fit - Results

In the following subsections, the results of the time resolution and lifetime fitting procedure on "purified" data are presented. Each of the subsections corresponds to one of the nine analyzed channels. The following quality cuts were used for event selection

- `isSignal = 1`
- `TagVpVal > 0.01`
- `chiProb > 1e-05`

- `DeltaTErr` < 1.5
- `|qrMC|` > 0.01

The supplementary cut on the `DeltaTErr` select out events with relatively low values of the uncertainty on the Δt variable, whereas the `chiProb` variable cut is a signal-side equivalent of the imposed `TagVpVal` constraint. Limitation of `|qrMC|` values ensures quality result of the tagging procedure by selecting events with correctly matched flavors of the neutral B -mesons. The effect of the additional cuts on the number of events available for analysis gives an indication of the quality of the data reconstructed. This comparison expressed in numbers can be found in Table 4.4.

Channel	#simulated events	#events in prelim. studies sample	#events w/ quality cuts
B0toJPsiKStoEE	1 000 000	362 258	252 432
B0toJPsiKStoMuMu	1 000 000	607 946	424 191
B0toPiDPtoK2Pi	1 000 000	550 545	397 374
B0toPiDStoK2Pi	500 000	276 409	183 698
B0toPiDStoK4Pi	500 000	239 698	117 457
BPtoJPsiKtoEE	1 000 000	392 174	316 627
BPtoJPsiKtoMuMu	1 000 000	664 773	536 752
BPtoPiD0toK3Pi	1 000 000	470 119	320 196
BPtoPiD0toKPi	2 000 000	1 269 453	1 004 603

Table 4.4: # events in the signal MC dataset

No tag- nor signal- side vertexing constraint was used. The following plots consist of the main fit result, a ratio, and a residual plot. The second plot illustrates the ratio of the MC value in the particular bin to the resulting fitting function value. The bottom-row figure depicts a value-fit pull defined in a following way:

$$f_i^{pull}(\Delta t) = \frac{\frac{v_i}{w_i} - 1}{\frac{v_i}{w_i}} \quad (4.6)$$

where v_i ($i \in \{0, \dots, 200\}$) denotes a number of events in the i -th bin and w_i stands for the value given by the fit for the same bin.

4.4.1 B0toPiDPtoK2Pi

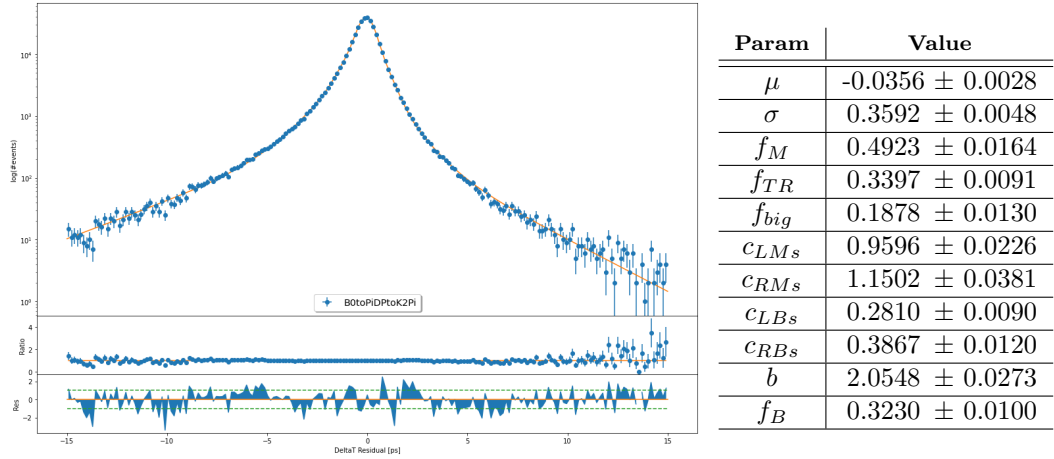
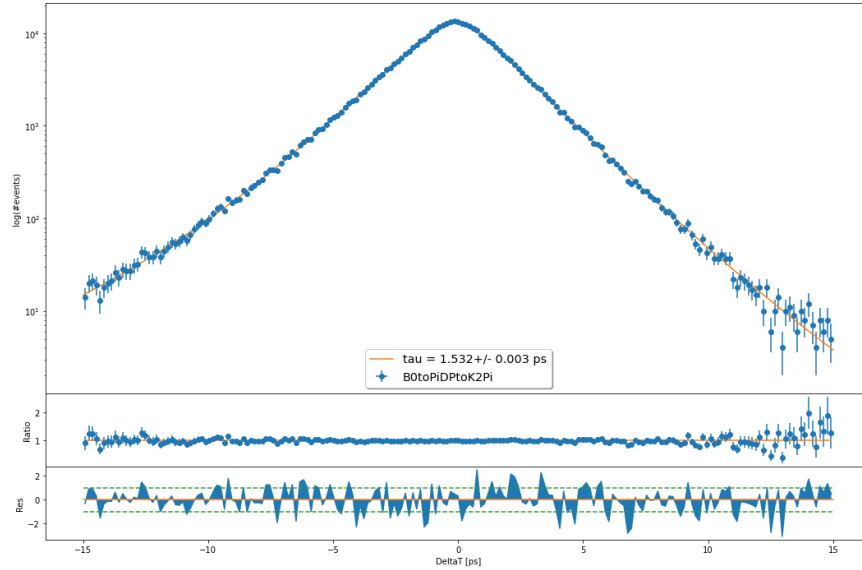


Figure 4.1: Δt_{res} fit results for the B0toPiDPtoK2Pi channel

The Figure 4.1 shows that the resolution function successfully managed to describe the decay-time residual spectrum in the core part. The fitted values of B -meson lifetime support this statement as it deviates from the number used for MC generation by $3\text{-}\sigma$. The distribution is slightly asymmetric, which explains the differences in the $c_{L/R}$ coefficients values, especially in the case of the broader Gaussian distribution. Discrepancies between the fitting function and the residual histogram values start appearing near the outer end-tails, which are lower in statistics.



Fitted Variable	τ_B [ps]	$\frac{\tau - \tau_{MC}}{\sigma_\tau}$
DeltaT	1.532 ± 0.003	2.3
MCDeltaT	1.531 ± 0.002	3.0

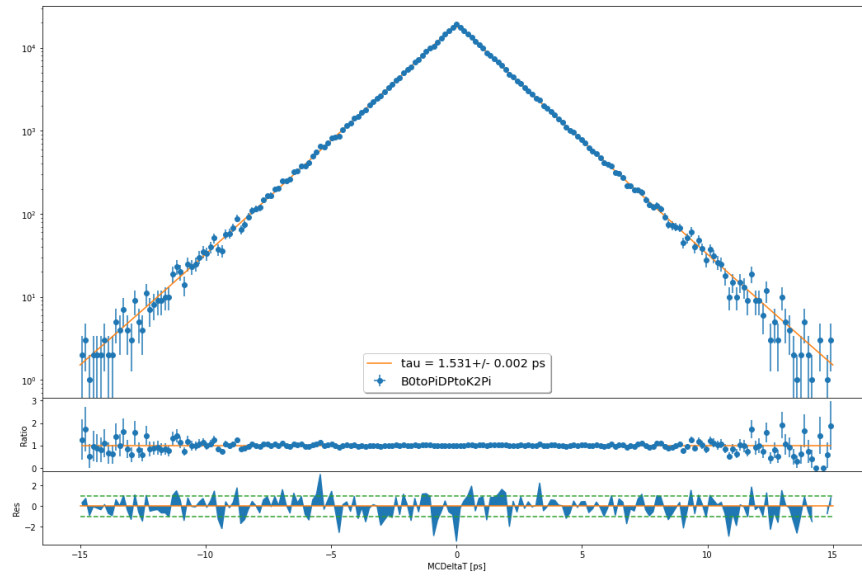


Figure 4.2: Δt (on the top) and Δt_{MC} (on the bottom) lifetime fit for the B0toPiDPtoK2Pi channel. The fitted values of τ_B can be found in the center table.

The proper-decay time difference fit with fixed parameter values matches the DeltaT spectrum in full domain. The determined lifetime τ_B values from the MCDeltaT and DeltaT agree within statistical uncertainty.

4.4.2 B0toPiDStoK2Pi

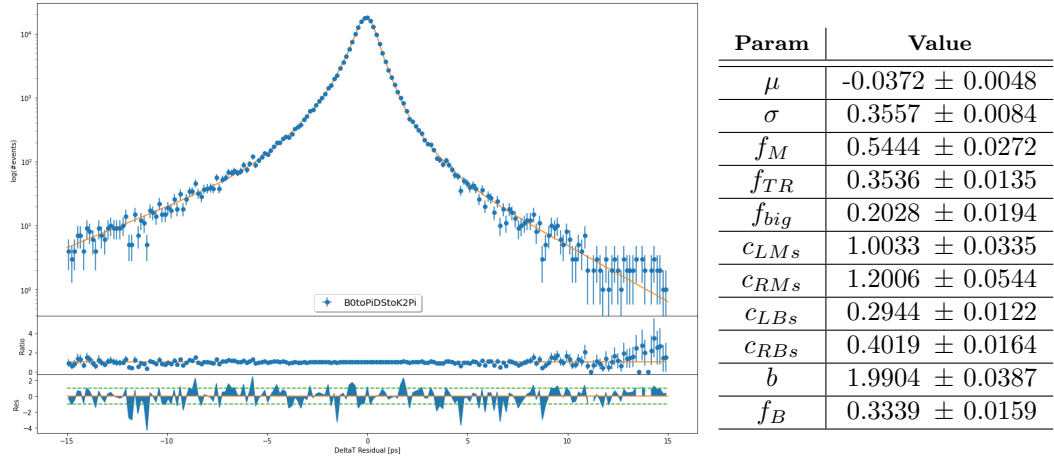
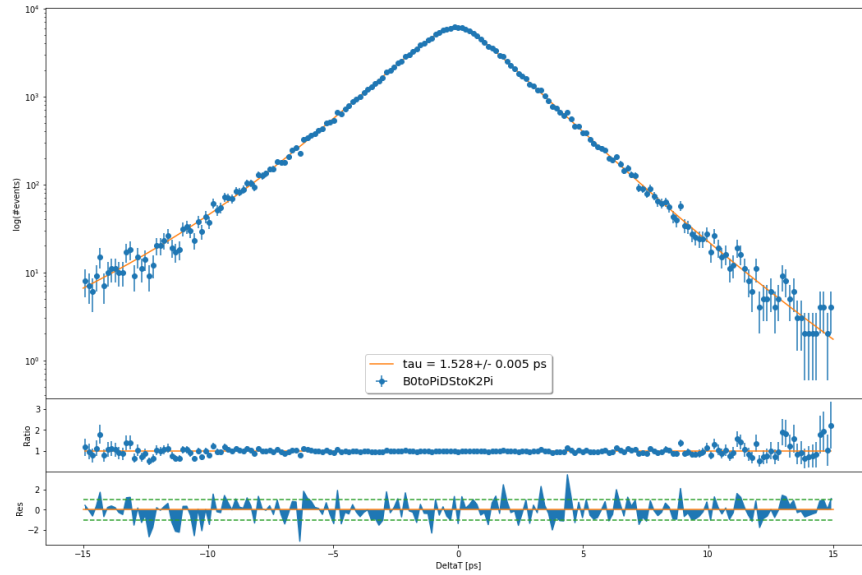


Figure 4.3: Δt_{res} fit results for the B0toPiDStoK2Pi channel

Despite the sample being half-size when compared with the B0toPiDPtoK2Pi channel, the fitting function again follows the histogram pattern without noticeable issues in the central region. A slight asymmetry of the spectra is present again. The discrepancy in the right end tail part of the fit becomes more pronounced in the pictorial representation, however, it is not reflected dramatically in the resulting parameter values. These precisely match the parameters observed from the first fit within a $1\text{-}\sigma$ interval of uncertainty, except for the main Gaussian fraction, which slightly deviates from this trend.



Fitted Variable	τ_B [ps]	$\frac{\tau - \tau_{MC}}{\sigma_\tau}$
DeltaT	1.528 ± 0.005	0.6
MCDeltaT	1.531 ± 0.004	1.5

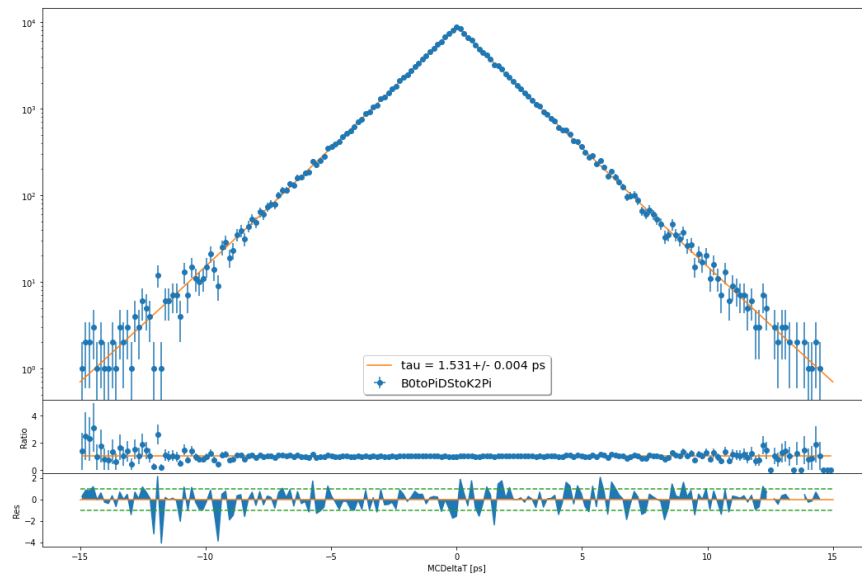


Figure 4.4: Δt (on the top) and Δt_{MC} (on the bottom) lifetime fit for the B0toPiDStoK2Pi channel. The fitted values of τ_B can be found in the center table.

The lifetime value agrees with the expected $\tau_{MC} = 1.525\text{ps}$ for a neutral B^0 -decay mode within the statistical uncertainty. The fitted values of lifetime based on the DeltaT and MCDeltaT spectra are precise and match almost exactly.

4.4.3 B0toPiDStoK4Pi

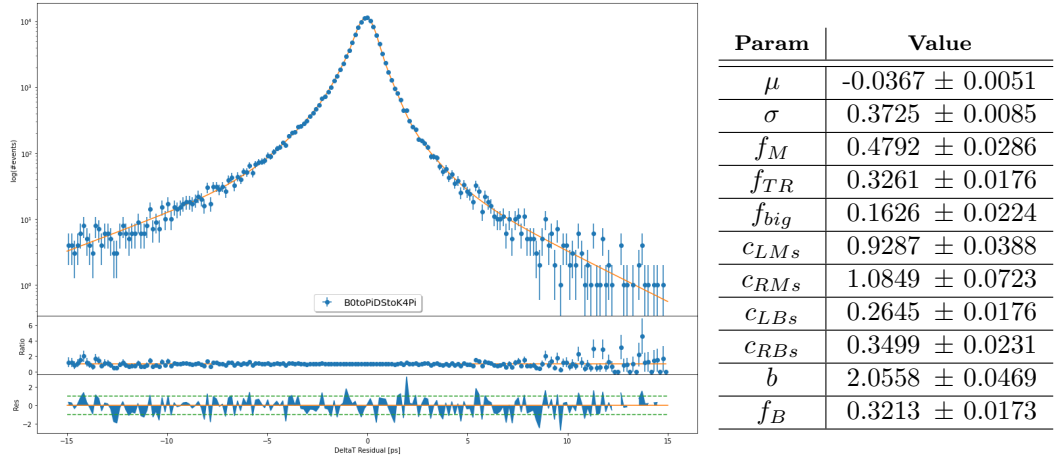
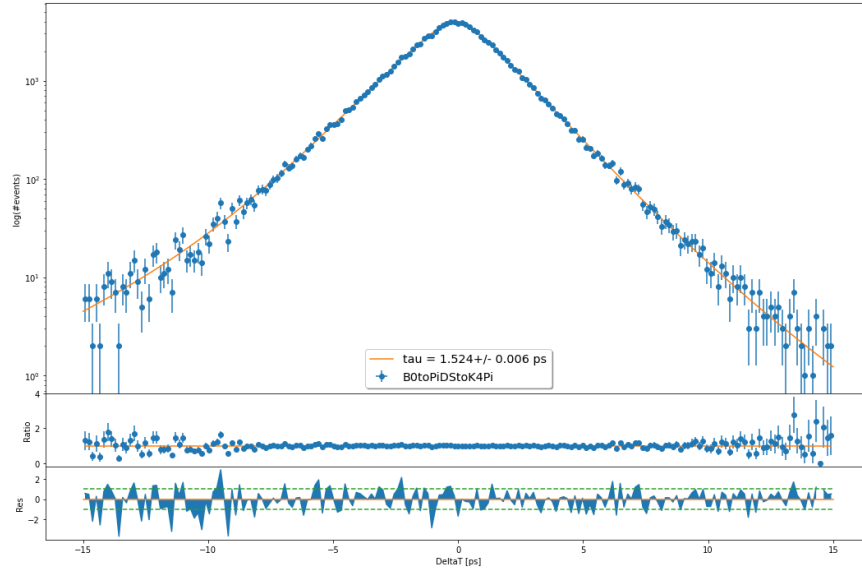


Figure 4.5: Δt_{res} fit results for the B0toPiDStoK4Pi channel

Kinematically challenging mode because of a higher number of particles in the final state has the lowest statistics of all channels. The central region around zero is described without greater issues, however the in the low-populated areas. As can be seen from the `DeltaT` and `MCDeltaT` plots, the statistical uncertainty grows significantly for the tails and the fit quality worsens. In general, the parameter values follow a similar trend as the previous neutral decay modes.



Fitted Variable	τ_B [ps]	$\frac{\tau - \tau_{MC}}{\sigma_\tau}$
DeltaT	1.524 ± 0.006	-0.2
MCDeltaT	1.523 ± 0.005	-0.4

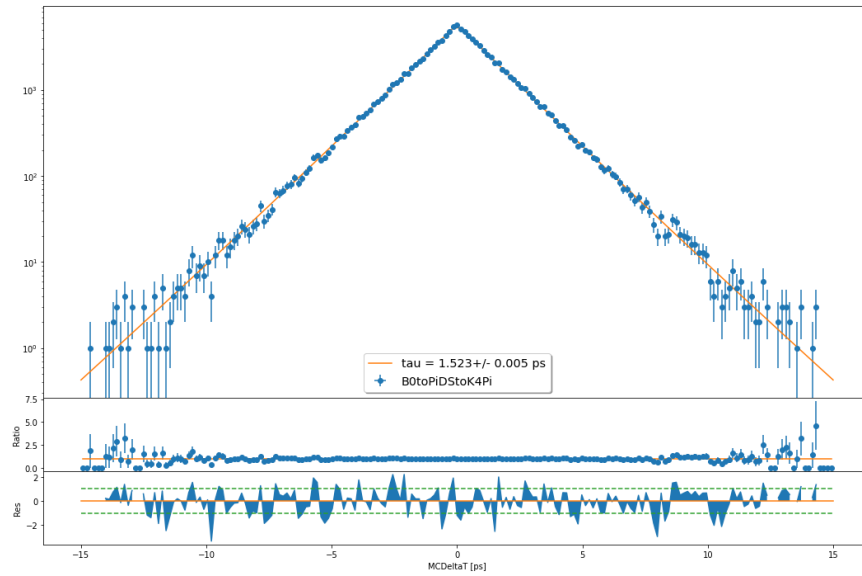


Figure 4.6: Δt (on the top) and Δt_{MC} (on the bottom) lifetime fit for the B0toPiDStoK4Pi channel. The fitted values of τ_B can be found in the center table.

The central value of the interval of statistical uncertainty agrees with the anticipated result. The obtained result experienced the most significant change when the quality cuts were applied.

4.4.4 B0toJPsiKStoMuMu

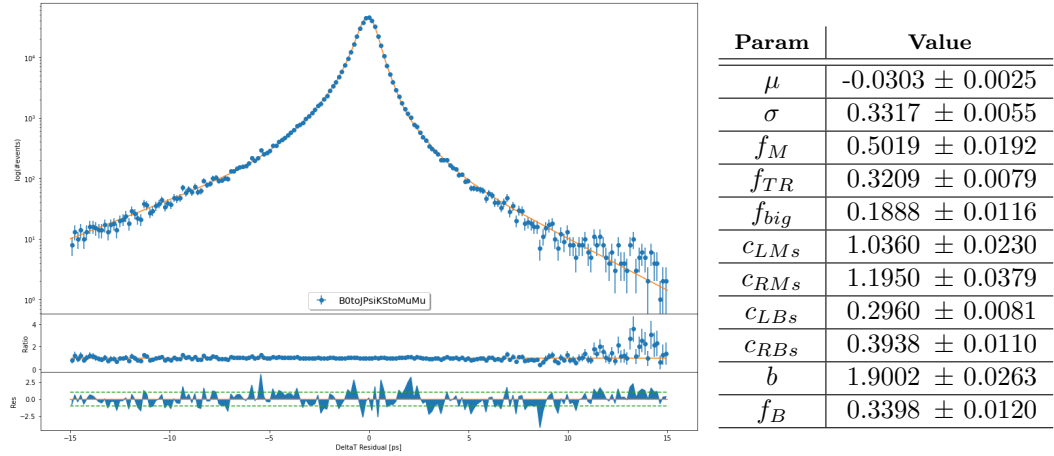
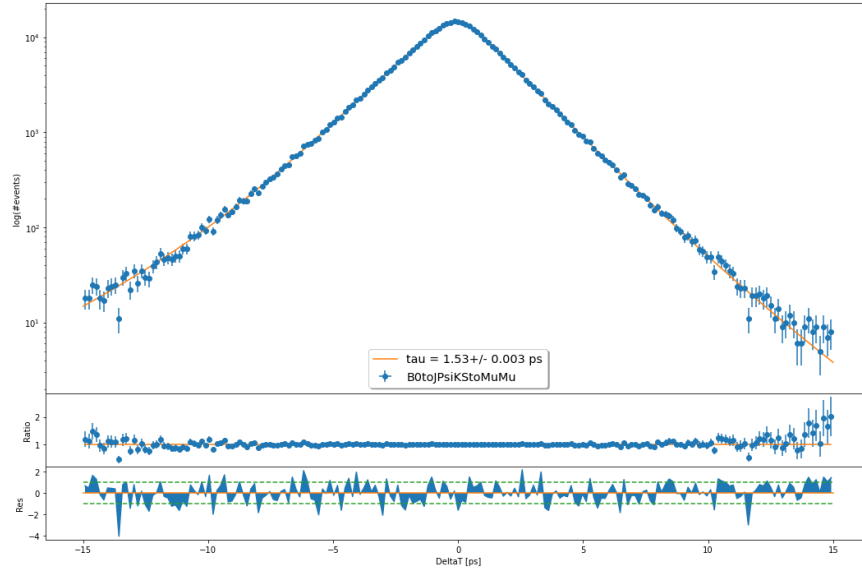


Figure 4.7: Δt_{res} fit results for the B0toJPsiKStoMuMu channel

Fits of this kinematically very clean channel reconstructed using the muonic pair nicely describe the spectra. Thanks to the relatively high statistics, the resolution function and the convolution show good agreement with the histogram values even in the tail parts. A slightly different fractional distribution of contributions by individual terms of the resolution function can be observed in the parameter values. The fitted μ parameter value indicates a subtly more centered distribution. The scaling parameter b slightly drops below 2 in comparison with the previous neutral decay modes.



Fitted Variable	τ_B [ps]	$\frac{\tau - \tau_{MC}}{\sigma_\tau}$
DeltaT	1.530 ± 0.003	1.7
MCDeltaT	1.528 ± 0.002	1.5

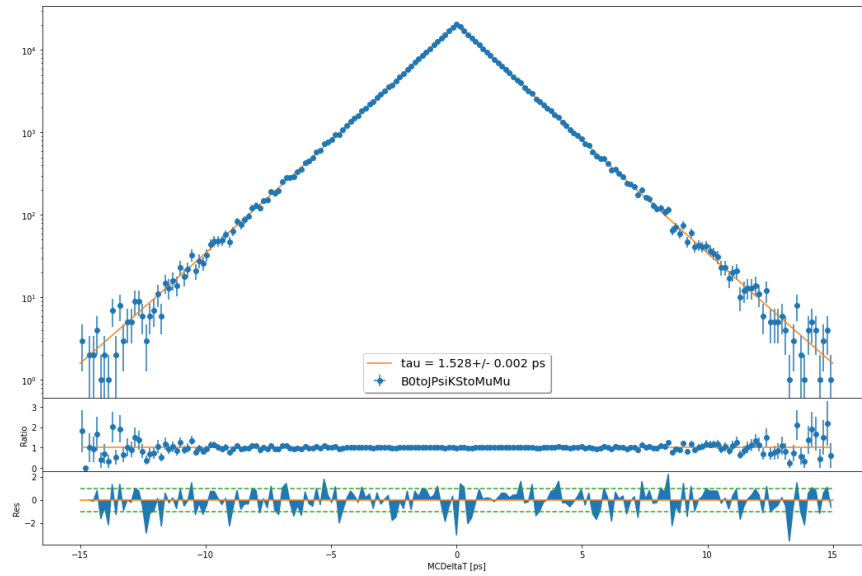


Figure 4.8: Δt (on the top) and Δt_{MC} (on the bottom) lifetime fit for the $B_0 \rightarrow J\psi K S \rightarrow \mu \mu$ channel. The fitted values of τ_B can be found in the center table.

Lifetime values obtained from fits of both variables lay within a $2\text{-}\sigma$ interval from the reference value as the statistical uncertainty decreases in comparison with the small dataset corresponding to the $B_0 \rightarrow \pi D S \rightarrow K 4\pi$ channel.

4.4.5 B0toJPsiKStoEE

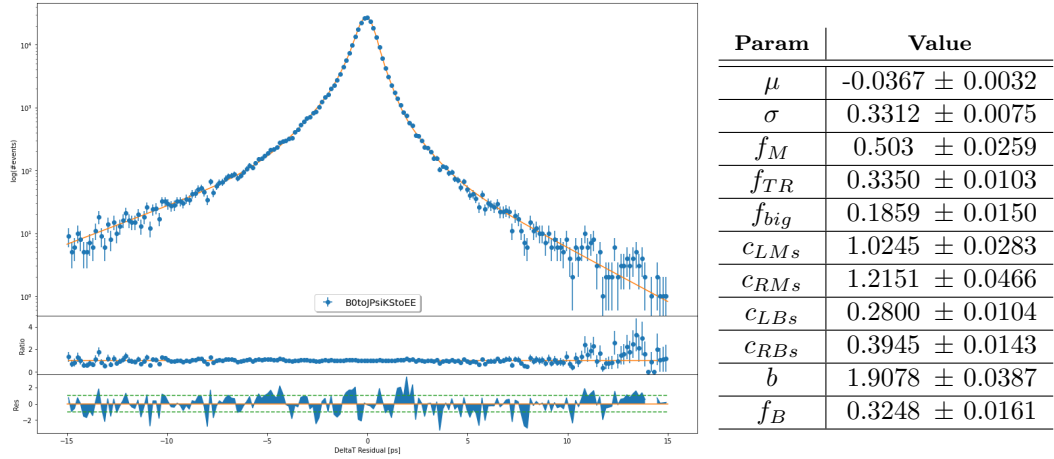
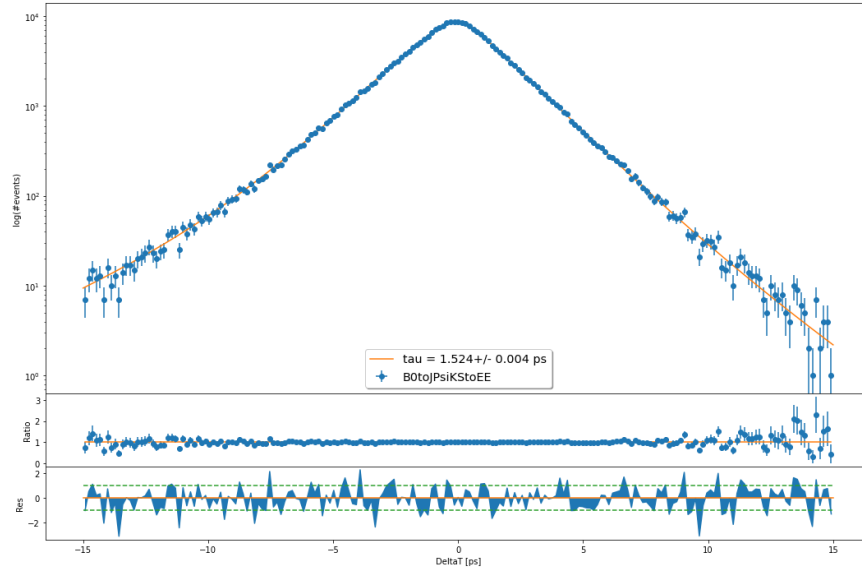


Figure 4.9: Δt_{res} fit results for the B0toJPsiKStoEE channel

Just like the previous channel, the B0toJPsiKStoEE is a favorable mode due to its lower background. The MC simulated data and the used functions agree, and no significant deviations are observed. The less populated tail regions do not exhibit higher uncertainties than for other channels. A deeper drop on the right side of the residual spectra is observed again. Determined values of parameter are consistent with other neutral channels. The b scaling factor exhibits lower value as did for the B0toJPsiKStoMuMu mode.



Fitted Variable	τ_B [ps]	$\frac{\tau - \tau_{MC}}{\sigma_\tau}$
DeltaT	1.524 ± 0.004	-0.3
MCDeltaT	1.523 ± 0.003	-0.7

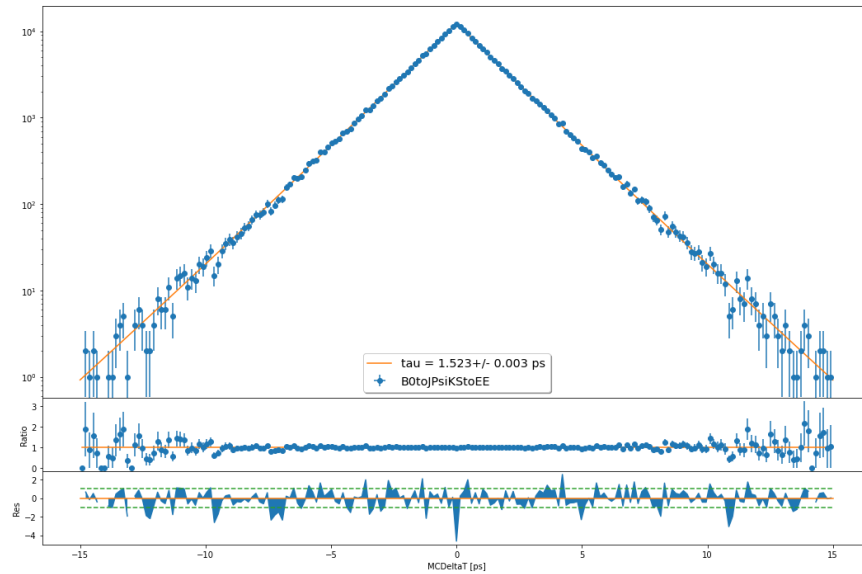


Figure 4.10: Δt (on the top) and Δt_{MC} (on the bottom) lifetime fit for the B_0 to $J\Psi$ KStoEE channel. The fitted values of τ_B can be found in the center table.

The central lifetime values of the uncertainty interval are slightly lower than the expected number but agree with the anticipated result in terms of statistics.

4.4.6 BPtoJPsiKtoMuMu

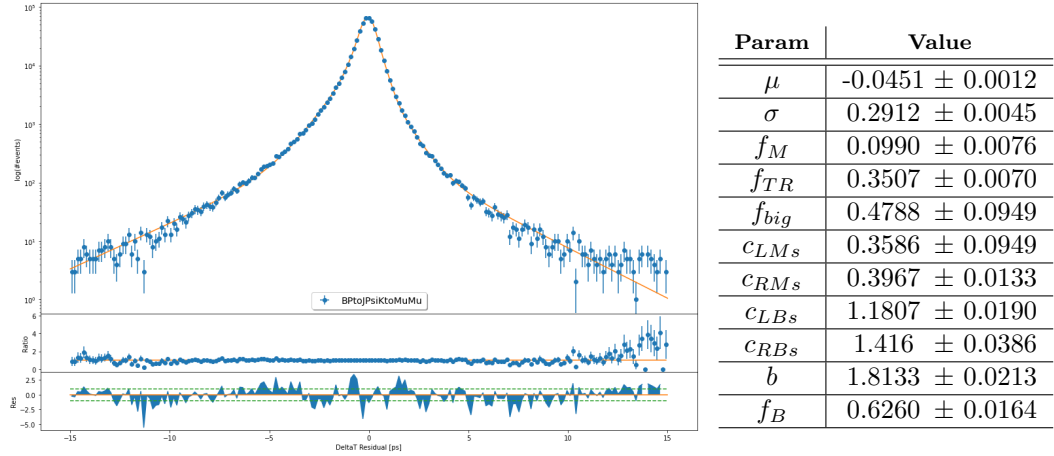
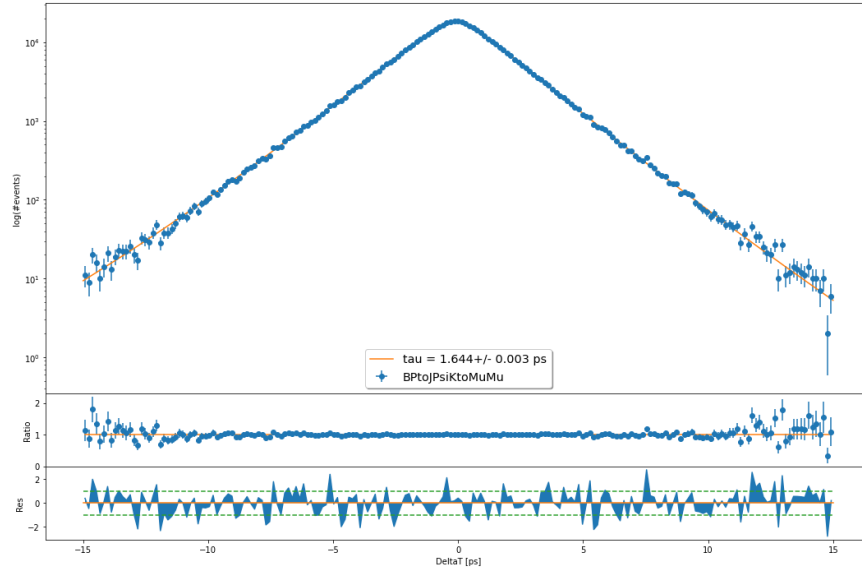


Figure 4.11: Δt_{res} fit results for the BPtoJPsiKtoMuMu channel

As can be seen in the Figure (4.11), the resolution function succeeded in describing a decay channel corresponding to a positively charged B -meson. All presented plots show agreement between the fitting function and data. The less-populated tail regions, especially on the right side of the plot, deviate from the fitted functional dependence. An unusual rise can be observed on the very right end of the fitted region. In terms of the parameter values, it can be seen that contribution of the wider Gaussian kernel became more pronounced, whereas the main-core fraction value dropped. The corresponding c factors also follow this trend. In comparison with the neutral decay modes, the bigger Gaussian width scaling factor b is smaller.



Fitted Variable	τ_B [ps]	$\frac{\tau - \tau_{MC}}{\sigma_\tau}$
DeltaT	1.644 ± 0.003	2.0
MCDeltaT	1.641 ± 0.002	1.5

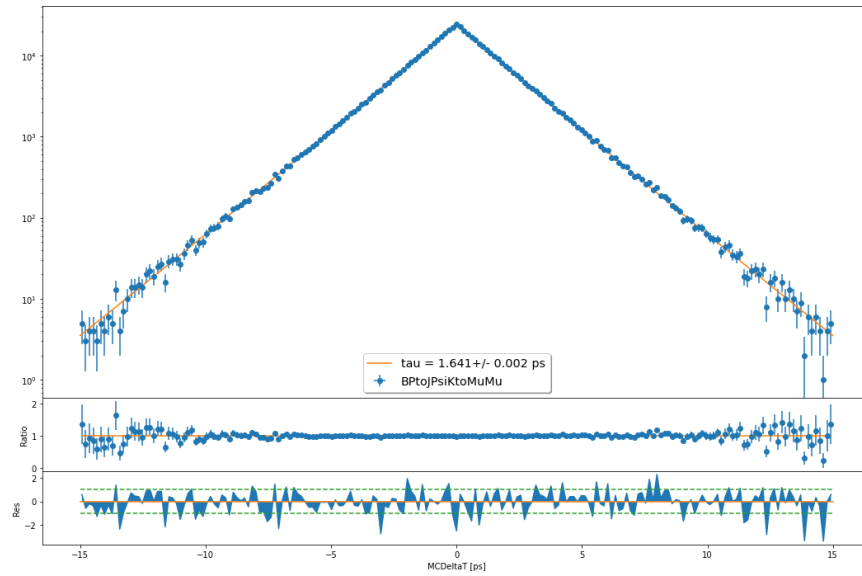


Figure 4.12: Δt (on the top) and Δt_{MC} (on the bottom) lifetime fit for the BPT0JPsiKtoMuMu channel. The fitted values of τ_B can be found in the center table.

The obtained values of lifetime lay within a $2\text{-}\sigma$ wide interval from the expected value τ_{B^+} used for generation of the MC sample.

4.4.7 BPtoJPsiKtoEE

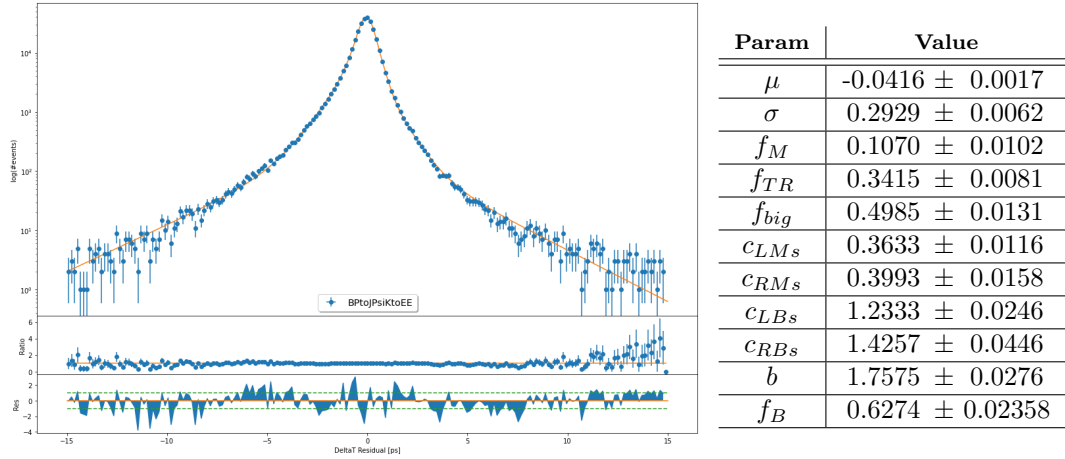
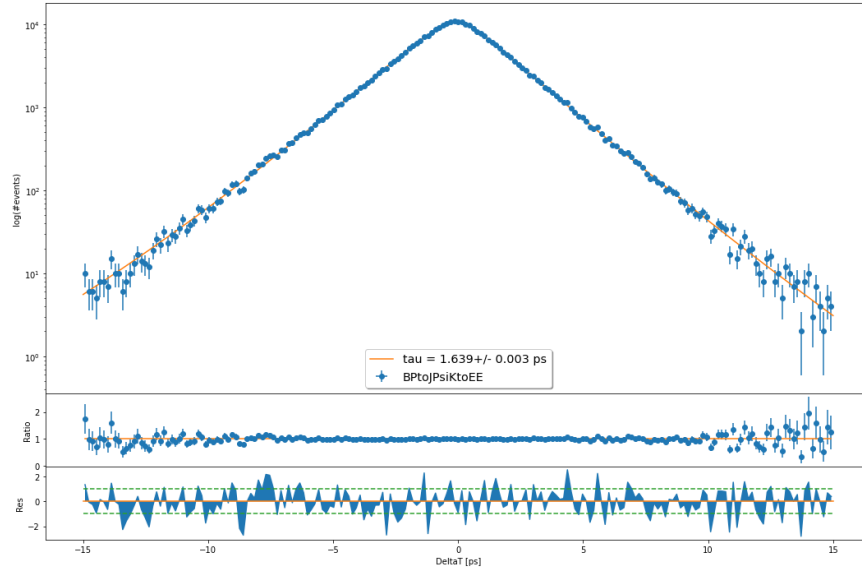


Figure 4.13: Δt_{res} fit results for the BPtoJPsiKtoEE channel

In comparison with the BPtoJPsiKtoMuMu the quality of the fit for the BPtoJPsiKtoEE channel seems to worsen due to lower statistics in the outer parts of the spectrum. The peak of the distribution is fully described by the fitting function. At the base of the distribution around the values of residual ~ 5 ps the fitting curve slightly parts from data to compensate the statistical fluctuations in tails. A discrepancy in this area is observed mainly for the fits exhibiting higher contribution from the wider Gaussian term. The rise on the right end side of the spectra is not as distinct for this channel. The width scaling factor b stays smaller than for neutral channels.



Fitted Variable	τ_B [ps]	$\frac{\tau - \tau_{MC}}{\sigma_\tau}$
DeltaT	1.639 ± 0.004	-0.8
MCDeltaT	1.639 ± 0.003	0.3

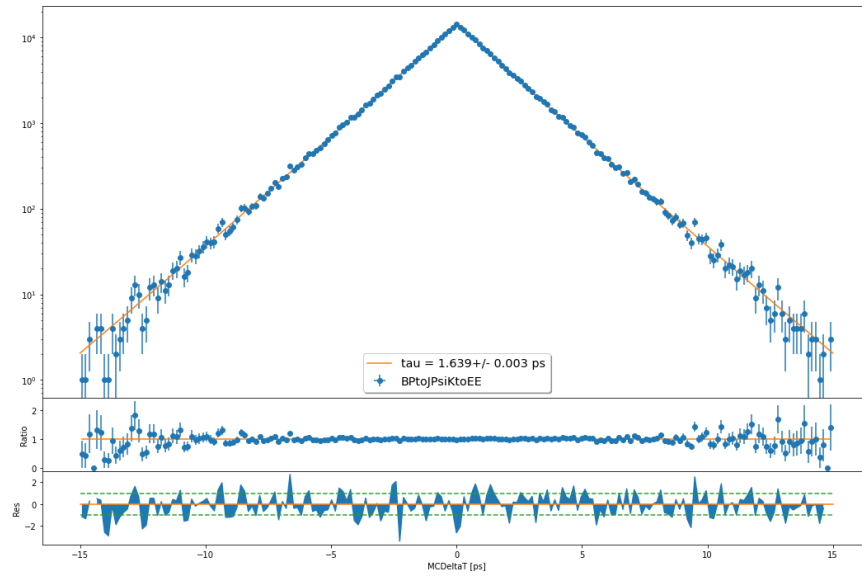


Figure 4.14: Δt (on the top) and Δt_{MC} (on the bottom) lifetime fit for the BPT0JPsiKtoEE channel. The fitted values of τ_B can be found in the center table.

The lifetime values extracted from the fits lay within a $1\text{-}\sigma$ uncertainty interval and therefore manifest good agreement between the fitting curve and MC data.

4.4.8 BPtoPiD0toKPi

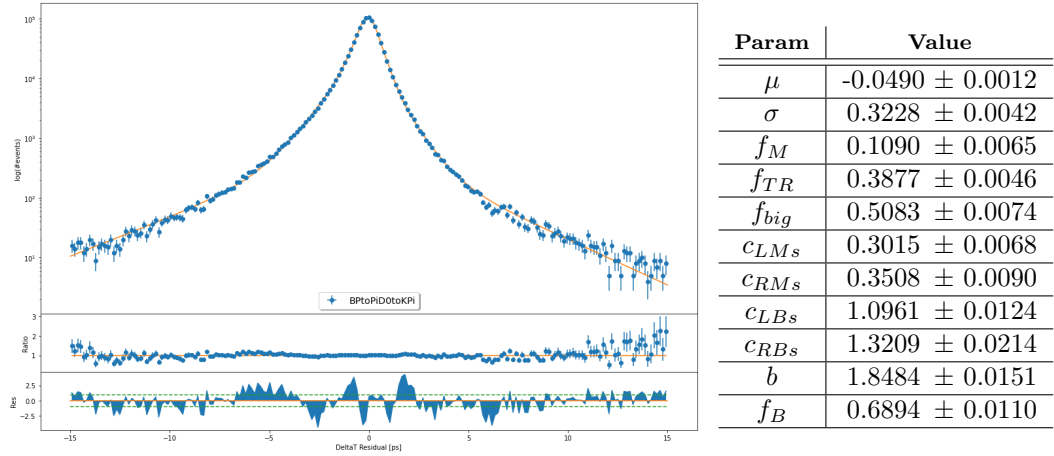
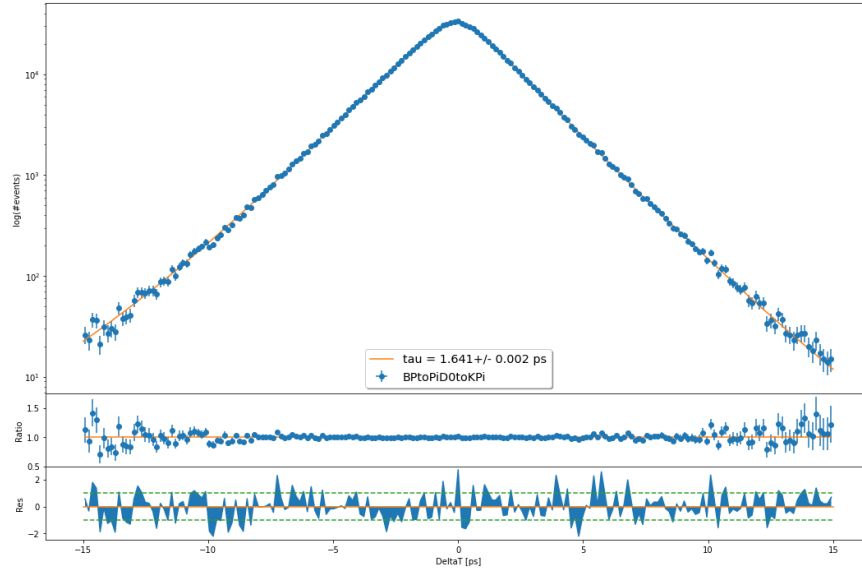


Figure 4.15: Δt_{res} fit results for the BPtoPiD0toKPi channel

The highest number of events was analyzed for the BPtoPiD0toKPi channel. The fitting curve successfully manages to describe the residual distribution even in the less populated tail regions. A slight deviation around the ~ 5 ps region can be observed again, as is also suggested by the value of the corresponding c_{RBs} parameter.



Fitted Variable	τ_B [ps]	$\frac{\tau - \tau_{MC}}{\sigma_\tau}$
DeltaT	1.641 ± 0.002	1.5
MCDeltaT	1.639 ± 0.002	2.0

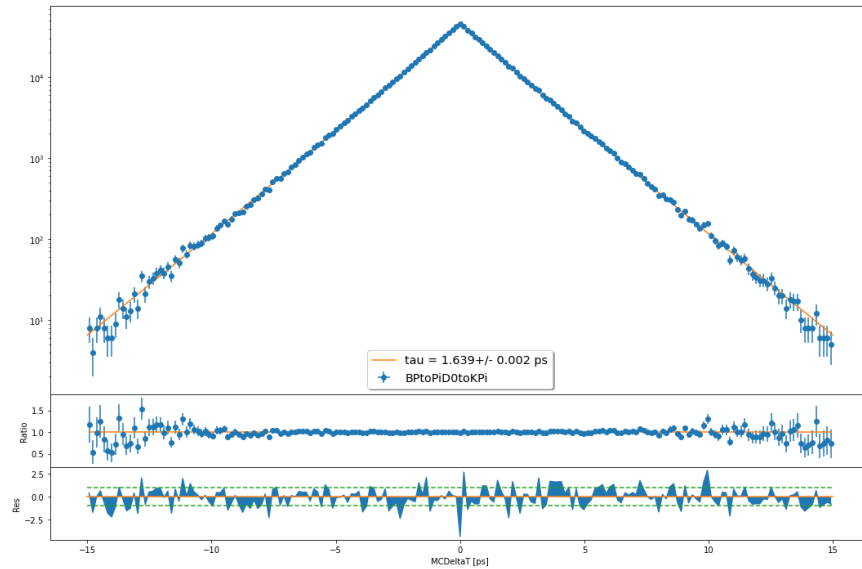


Figure 4.16: Δt (on the top) and Δt_{MC} (on the bottom) lifetime fit for the BPToPiD0toKPi channel. The fitted values of τ_B can be found in the center table.

The B^+ lifetimes extracted from the MCDeltaT and DeltaT fits do not deviate from the expected value $\tau_{B^+} = 1.638$ ps and are accurate within no more than a $2\text{-}\sigma$ wide uncertainty interval.

4.4.9 BPtoPiD0toK3Pi

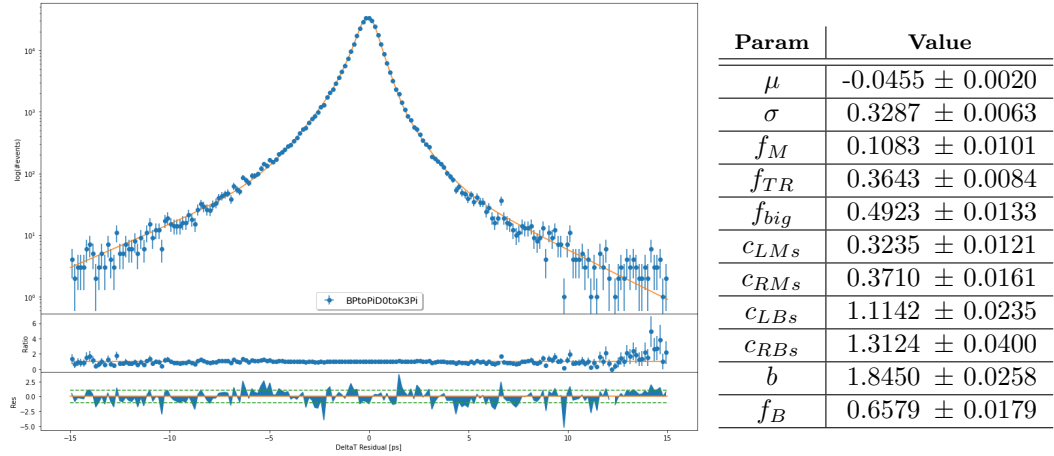
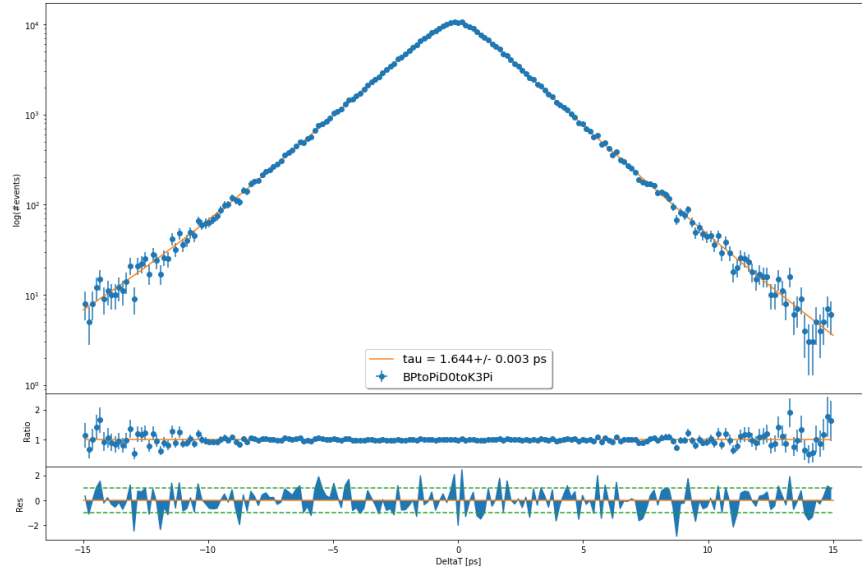


Figure 4.17: Δt_{res} fit results for the BPtoPiD0toK3Pi channel

The universally observed worse quality of fit at the right end of the spectra is again visible. The parameter values for this positively charged decay mode suggest a bigger contribution from the wider Gaussian term. The convoluted functions copy the `MCDeltaT` and `DeltaT` spectra nicely throughout the entire fitted region including the end-tail parts.



Fitted Variable	τ_B [ps]	$\frac{\tau - \tau_{MC}}{\sigma_\tau}$
DeltaT	1.644 ± 0.003	0.3
MCDeltaT	1.644 ± 0.002	2.0

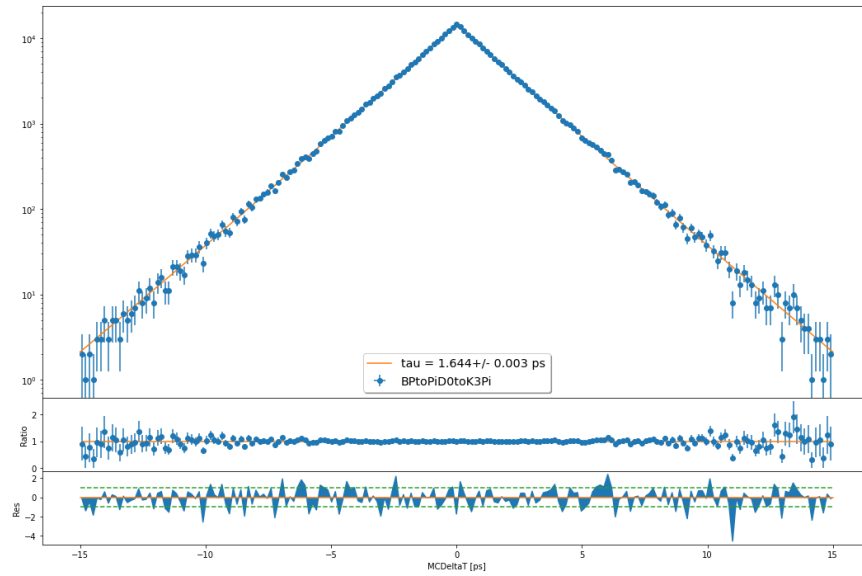


Figure 4.18: Δt (on the top) and Δt_{MC} (on the bottom) lifetime fit for the BPToPiD0toK3Pi channel. The fitted values of τ_B can be found in the center table.

The fitted values of lifetime agree precisely between the fits of MCDeltaT and DeltaT and both accurately match the expected value within a $2\text{-}\sigma$ interval.

4.4.10 Preliminary Results - New MC Dataset

Channel	Without quality cuts		With quality cuts	
	τ_B [ps]	$\frac{\tau - \tau_{MC}}{\sigma_\tau}$	τ_B [ps]	$\frac{\tau - \tau_{MC}}{\sigma_\tau}$
B0toPiDPtoK2Pi	1.530 ± 0.003	1.7	1.531 ± 0.003	2.0
B0toPiDStoK2Pi	1.525 ± 0.004	0.0	1.529 ± 0.004	1.0
B0toPiDStoK4Pi	1.514 ± 0.004	-2.8	1.519 ± 0.005	-1.2

Table 4.5: B -meson τ values from a DeltaT fit

The results for the preliminary studies performed using a smaller MC sample processed by a recent version of the software can be found in Table 4.5 and Table 4.6. Fits were performed using the same form of resolution function as in the case of the older MC dataset. The additional quality cuts changed the obtained fit results within the statistical uncertainty range of $1\text{-}\sigma$.

Channel	Without quality cuts		With quality cuts	
	τ_B [ps]	$\frac{\tau - \tau_{MC}}{\sigma_\tau}$	τ_B [ps]	$\frac{\tau - \tau_{MC}}{\sigma_\tau}$
B0toPiDPtoK2Pi	1.531 ± 0.002	3.0	1.532 ± 0.002	3.5
B0toPiDStoK2Pi	1.530 ± 0.003	1.7	1.530 ± 0.003	1.7
B0toPiDStoK4Pi	1.520 ± 0.004	-1.3	1.521 ± 0.004	-1.0

Table 4.6: B -meson τ values from a MCDeltaT fit

5. Discussion

The first section of the analysis part of this work presents the Monte Carlo and Data Comparison studies performed to validate various vertexing constraint options and newly introduced BeamSpot calibration. Validation results of the BeamSpot calibration and the discussion of its impact on the reconstruction quality are provided.

Based on comparing similar studies performed in the Summer 2020 and Fall 2020 periods, the author analyzed the results obtained for various combinations of applied constraints. Validation results of the BeamSpot calibration and the discussion of its impact on the reconstruction quality is provided.

The Summer 2020 plots justify the decision of the TDCPV working group not to use any of the more sophisticated vertexing constraints. In the Figure 3.3 one can observe the discrepancies between the data and MC simulation. The shapes of the dependencies do not match. In the reconstructed data spectra, additional peaks and fluctuations can be observed. Quantitatively, the size of the uncertainties decreases, however, the interpretation of the observed results is not unequivocally clear. Therefore, so as not to incorporate an unnecessary potential source of systematic uncertainty into the analysis, the vertexing constraints "IP" and "Tube" were not used for further analysis performed in the latter half of 2020.

According to the Figures 3.4 - 3.6 the new time-dependent BeamSpot calibration seems to be having a positive effect on the decay vertex reconstruction quality. This impact is observed for both the tag as well as the signal event side. The uncertainties on all studied variables lowered, and the improvement was most pronounced for y -coordinate associated elements. This observed pattern seems plausible as the BeamSpot calibration corrects the y -dimension of the luminous region size most noticeably. The combination of the "Tube" constraint on the tag-side and the "IP - pointing" constraint on the signal event side seems to be providing the most promising results. For further and more definite conclusions, analysis of the new independent Monte Carlo 14 campaign is necessary as it will be processed using the current version 5 of the `basf2` software. The parameters of the luminous region for the Monte Carlo 14 campaign are based on the BeamSpot parameters obtained by the "new" BeamSpot calibration method and, therefore, the simulated luminous region better matches the one in data.

However, there is one remaining issue. The data beam conditions vary with time, whereas in the run-independent MC, for example, the BeamSpot size is by definition constant in the whole sample. Therefore, a perfect agreement between data and run-independent MC will never be achieved.

The core part of the analysis deals with the consistency and validation studies of the time resolution function. A simplified version of the proper time resolution function(the full version of which is currently under study and in the stage of development) was used for this analysis. As a preliminary step, the resolution function was applied to MC data samples processed as described in the MC-Data comparison analysis section. Datasets were available for nine different decay modes, five of which corresponded to neutral B^0 -meson and four to charged B^+ decay channels.

A few quality cuts were applied to these simulated sets to filter out the events

for which the tag-side vertexing procedure failed (the `TagVpVal` cut) and select those with correctly reconstructed particles (the cut on the `isSignal` variable).

The analysis was performed in three steps, first, the resolution function (of the form described in 4.5) was applied to the Δt_{res} variable as explained in 4.3. The values of 11 free-floating parameters of this fit were then fixed for further application. This fixed-parameter form of the resolution function was convolved with distribution describing the time-dependent evolution of proper decay time difference of the neutral $B\bar{B}$ meson pair (see 2.16). As the results in Table (4.2) show, the lifetime values obtained from the preliminary fit applied to the weakly constrained data for some channels considerably deviated from expected values used for the MC generation ($\tau_{B^0} = 1.525$ ps, $\tau_{B^+} = 1.638$ ps).

For this reason, the time resolution fit was repeated on the `MCDeltaT` variable. This helped determine whether the discrepancies were caused by the quality or processing of data or by the form of the resolution function itself. Since the same issue occurred in the Δt_{MC} fit (see Table 4.3, further quality cuts were imposed on the event selection. These are described in the Section(4.4).

The steps of the fitting procedure were replicated, and the summary of the results can be found in Table A.1 and Table A.2 in the Appendix A. The lifetime of B -mesons determined by this procedure accurately match the expected values within the uncertainty interval of 2σ . The values extracted from the fit of the `DeltaT` and `MCDeltaT` variables are very similar, which implies the studied resolution function works well. Pictorially, the fitted values for each of the parameters of the function for all 9 analyzed channels are compared in Figures 5.1 - 5.4.

Based on the plots illustrating the values of the μ , σ and the f_{TR} parameters do not show how explicit dependence on the charge of the decaying B meson. For these variables, the constant orange line in the center part of the figure represents the mean value of the fitted parameter across all nine channels. For all the remaining parameters, the plots also contain two green dashed lines representing average over all neutral and charged mode parameter values, correspondingly. For the neutral as well as charged mesons, the decay chains including D mesons and those proceeding via the $J/\psi K_s$ resp. $J/\psi K_s^*$ state, seem to agree more precisely within their respective categories in the case of σ and b parameters.

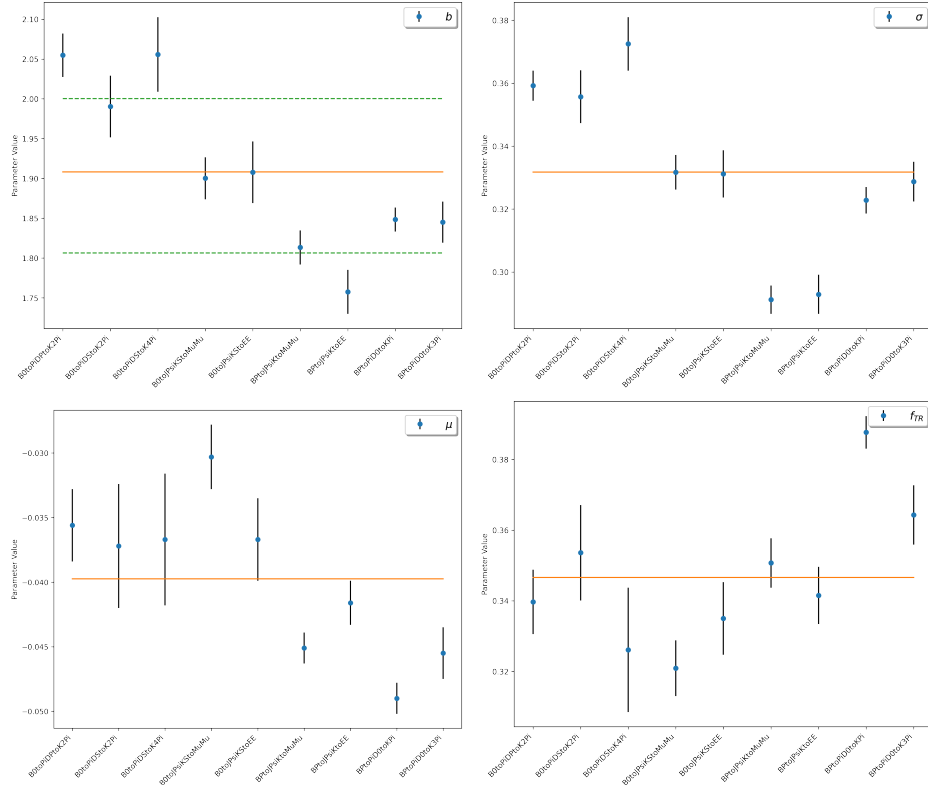


Figure 5.1: Time resolution function - fit results and parameter values. The orange line represents the mean value of all parameter values, whereas the green lines correspond to means over the neutral resp. charged channel parameter values.

On the other side, differences between the charged and neutral channels are noticeable in the case of f_M , f_{big} , f_B , and the c_{RM_s} , c_{LM_s} , c_{RB_s} , c_{LB_s} parameters. The size of the c parameters is correlated with the fractional representation of the main resp. wider Gaussian kernel.

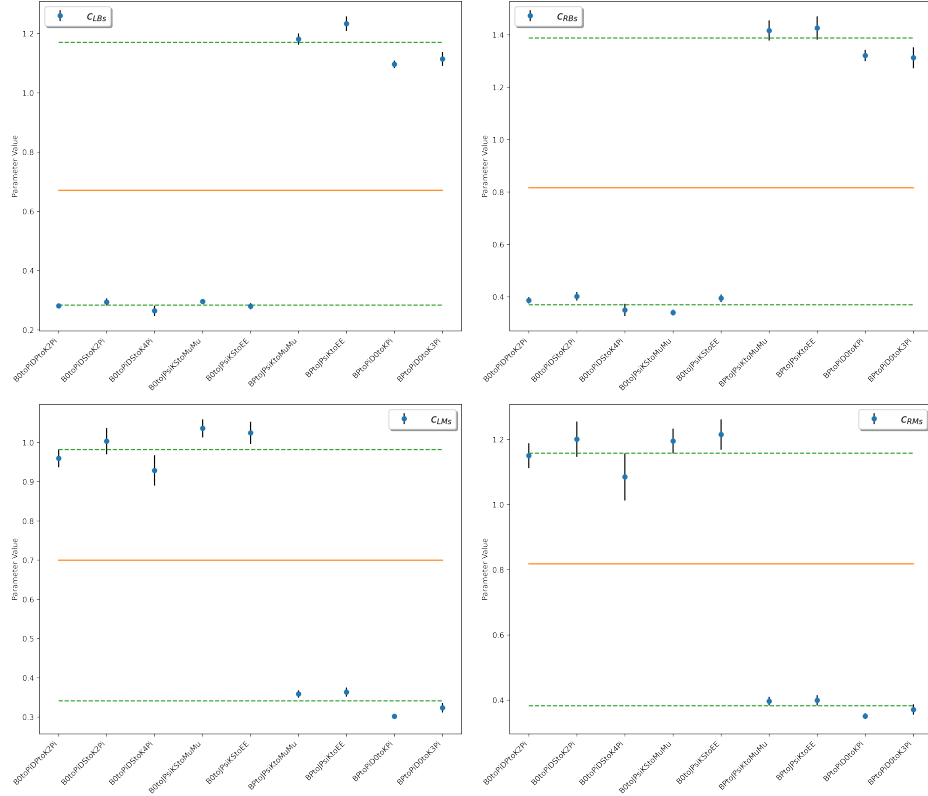


Figure 5.2: Time resolution function - fit results for the c parameter values. The orange line represents the mean value of all parameter values, whereas the green lines correspond to means over the neutral resp. charged channel parameter values.

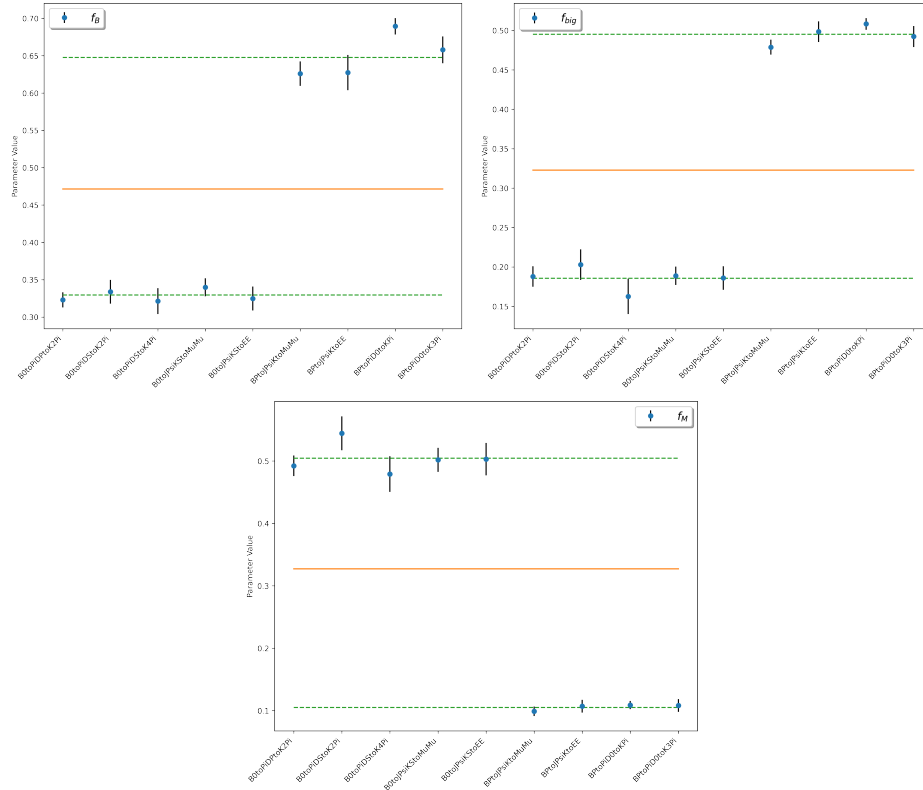


Figure 5.3: Time resolution function - fit results for the fraction parameter values. The orange line represents the mean value of all parameter values, whereas the green lines correspond to means over the neutral resp. charged channel parameter values.

Figure 5.4 illustrates agreement of determined lifetime values among neutral B^0 and charged B^+ meson decay modes, respectively. The precise congruence of the values obtained from DeltaT and MCDeltaT fits is also apparent.

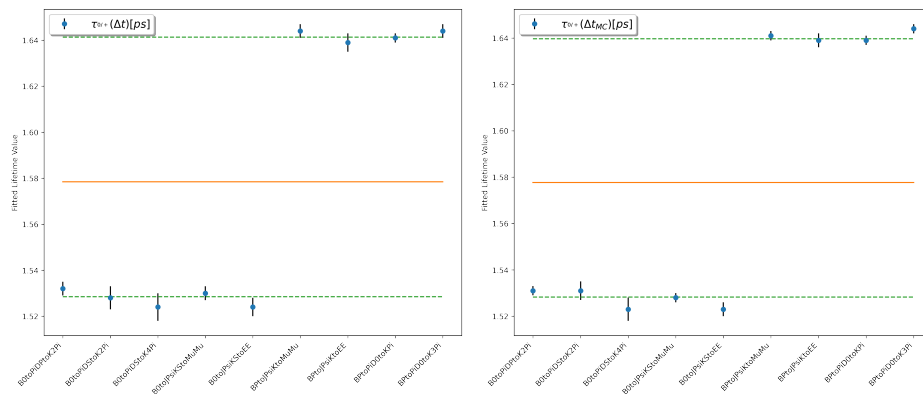


Figure 5.4: Time resolution function - lifetime fit results. The orange line represents the mean value over all lifetime values, whereas the green lines correspond to means over the neutral resp. charged channel lifetime values.

The quality cuts, however, are not usable for analysis on real data. The most very relevant effect comes from the quality cut (cut on the $|\text{qrMC}|$ value) related to the MC flavor- tagging quality indicator. It is necessary to wait for new data

sets, just like in the case of MC. These will be processed by the current software version, which also incorporated significant changes and improvements to the flavor tagging algorithm. The above-mentioned cut should be eliminated and the studies repeated solely utilizing cuts that are also available for real data.

To further support the proposition stating that software bugs and imperfections cause the observed discrepancies, the studies were also repeated on MC samples simulated using new software release 5. Results of the lifetime fit obtained from this short analysis are listed in Table 4.5 and Table 4.6. The results suggest the additional cuts do not need to be applied to data processed using version 5 of the `basf2` software. The effect of the more restrictive quality constraints is not uniform and could bring in more systematic bias. The fixes and corrections applied to the new software appear to have satisfactory effects on the data reconstruction quality.

In the context of the resolution function, the form used for the presented studies proved to be successful at determining the lifetime values. Seven of the total eleven parameters of the resolution function are similar across the neutral respectively charged channels. Their values could therefore be fixed to their average value, and the lifetime fit repeated. The analysis of such approach could help reduce the number of free-floating parameters. Another step might be trying to fix the values of the remaining parameters to the average values or fix their values across the subgroups within which they fluctuate only subtly.

Finally, the form of the resolution function should also be validated on real data. Due to the shortness of time and issues with the older `basf2` software release, the function has not been validated on currently available datasets. Future plans include validation using data processed by the current software version. The next step also incorporates augmenting the function by even-by-event dependence on the `DeltaTErr` uncertainty which would replace the currently constant value of σ parameter.

Conclusion

The importance of precise decay vertex reconstruction and time resolution information for time-dependent CP-violation, $B\bar{B}$ mixing and life-time studies is emphasized in this work. Several elements which influence the quality of proper time and position measurement are described, and tools for their improvement are validated and studied.

The first part of the thesis is devoted to the Belle II detector and SuperKEKB accelerator facility. The main characteristics and the fundamentals of operations of the detector building blocks are described. A brief timeline of the data-taking process divided into three Phases is provided, and the data acquisition system and the Belle II analysis software framework are shortly introduced. This described software is used for processing data and Monte Carlo samples essential for the analysis presented in further chapters.

The following section offers an overview of the basics of time-dependent CP-violation and asymmetry measurements in neutral meson systems. The measurement techniques employed by past experiments are introduced, and some of their achievements are illustrated. Theoretical background and motivation for employing proper time resolution function are provided.

The results presented in this work can be divided into two parts. The third chapter presents the outcome of MC/Data comparison studies for calibration constant and vertexing constraint validation. Subsequently, results of the analysis performed on new datasets processed by the author were juxtaposed with analysis performed in Summer 2020. Multiple combinations of utilizable vertexing constraints for B meson decay reconstruction were introduced and compared. In addition, new time-dependent calibration of the luminous region (BeamSpot) was subject to validation.

Consistency and universality of an introduced form or proper time resolution function are subject to testing and analysis. The ability of the function to accurately fit decay time residual spectra so as to determine lifetime values for neutral and charged B -mesons across nine different decay modes are studied. The software version used for MC sample processing is found to significantly impact the precision of the lifetime fit. Common patterns among fitted parameter values are observed for neutral and charged decay modes, respectively. These similarities and agreement across channel categories can be used to reduce the number of free-floating parameters and simplify the fitting procedure.

Bibliography

- [1] A. D. Sakharov. Violation of CP Invariance, C asymmetry, and baryon asymmetry of the universe. *Pisma Zh. Eksp. Teor. Fiz.*, 5:32–35, 1967.
- [2] Aubert B. et al. Study of time-dependent CP-violating asymmetries and flavor oscillations in neutral B decays at the $v(4S)$. *Physical Review D*, 66(3), Aug 2002.
- [3] Bevan A. et al. The Physics of the B Factories. *The European Physical Journal C*, 74(11), Nov 2014.
- [4] J. H. Christenson, J. W. Cronin, V. L. Fitch, and R. Turlay. Evidence for the 2π Decay of the K_2^0 Meson. *Phys. Rev. Lett.*, 13:138–140, Jul 1964.
- [5] Tanabashi M. et al. Review of Particle Physics, 2018-2019. *Phys. Rev. D*, 98:030001. 1898 p, 2018.
- [6] Kou E. et al. The Belle II Physics Book. *Progress of Theoretical and Experimental Physics*, 2019(12), Dec 2019.
- [7] A. J. Bevan. B factories. *Comptes Rendus Physique*, 13(2):145–151, Mar 2012.
- [8] Abe T. et al. Belle II Technical Design Report. *arXiv: High Energy Physics - Experiment*, 11 2010.
- [9] B. Oberhof. Precise measurements of CP violation in B decays at Belle II. *PoS*, HQL2018:004, 2018.
- [10] P.F. Harrison. An introduction to the BABAR experiment. *Nuclear Instruments and Methods in Physics Research Section A: Accelerators, Spectrometers, Detectors and Associated Equipment*, 368(1):81–89, 1995. Proceedings of the Third International Workshop on B-Physics at Hadron Machines.
- [11] J. Haba. KEKB and the BELLE experiment. *Nuclear Instruments and Methods in Physics Research Section A: Accelerators, Spectrometers, Detectors and Associated Equipment*, 368(1):74–80, 1995. Proceedings of the Third International Workshop on B-Physics at Hadron Machines.
- [12] Tajima H. et al. Proper-time resolution function for measurement of time evolution of B mesons at the KEK B-Factory. *Nuclear Instruments and Methods in Physics Research Section A: Accelerators, Spectrometers, Detectors and Associated Equipment*, 533(3):370–386, Nov 2004.
- [13] M. Bessner. The Belle II experiment: Status and prospects. *AIP Conference Proceedings*, 2249(1):030044, 2020.
- [14] B. Wang. The Belle II Experiment and SuperKEKB Upgrade. *J. Univ. Sci. Tech. China*, 46(7):617–624, 2016.
- [15] The Belle II collaboration. Belle II Luminosity. <https://confluence.desy.de/display/BI/Belle+II+Luminosity>. Accessed: 2021-05-19.

- [16] K. Akai, K. Furukawa, and H. Koiso. SuperKEKB collider. *Nuclear Instruments and Methods in Physics Research Section A: Accelerators, Spectrometers, Detectors and Associated Equipment*, 907:188–199, 2018. Advances in Instrumentation and Experimental Methods (Special Issue in Honour of Kai Siegbahn).
- [17] W. Wu and D. Summers. Luminosity and Crab Waist Collision Studies. In *48th Fermilab Users Organization Annual Meeting*, 5 2015.
- [18] A. Moll. *Comprehensive study of the background for the Pixel Vertex Detector at Belle II*. PhD thesis, Ludwig-Maximilians-Universität München, July 2015.
- [19] Simon F. et al. The Belle-II Pixel Vertex Detector at the SuperKEKB Flavor Factory. *Conf. Proc. C*, 0908171:563–565, 2009.
- [20] Paschen B. et al. Belle II pixel detector: Performance of final DEPFET modules. *Nuclear Instruments and Methods in Physics Research Section A: Accelerators, Spectrometers, Detectors and Associated Equipment*, 958:162222, 2020. Proceedings of the Vienna Conference on Instrumentation 2019.
- [21] Ch. Li. The data acquisition and trigger system of the Belle II experiment. *PoS*, EPS-HEP2015:258, 2016.
- [22] Dossett D. et al. Status of the calibration and alignment framework at the belle II experiment. *Journal of Physics: Conference Series*, 898:032032, oct 2017.
- [23] Dossett, D. and Seviar, M. Prompt calibration automation at Belle II. *EPJ Web Conf.*, 245:02016, 2020.
- [24] Kotchetkov D. et al. Front-end electronic readout system for the Belle II imaging Time-of-Propagation detector. *Nuclear Instruments and Methods in Physics Research Section A: Accelerators, Spectrometers, Detectors and Associated Equipment*, 941:162342, 2019.
- [25] M. Kobayashi and T. Maskawa. CP Violation in the Renormalizable Theory of Weak Interaction. *Prog. Theor. Phys.*, 49:652–657, 1973.
- [26] R. F. Lebed. Relating CKM parametrizations and unitarity triangles. *Physical Review D*, 55(1), 1 1997.
- [27] Abe K. et al. Improved measurement of CP-violation parameters $\sin 2\phi_1$ and $|\lambda|$, B meson lifetimes, and $B^0\text{-}\bar{b}^0$ mixing parameter Δm_d . *Phys. Rev. D*, 71:072003, Apr 2005.
- [28] R. Žlebčík. Private communication with thesis supervisor, 2021.
- [29] Belle II Computing. <https://www2.kek.jp/proffice/archives/feature/2010/BelleIIComputing.html>. Accessed: 2021-05-03.
- [30] Belle II - Computing. <https://belle2.jp/computing/>, 2021. Accessed: 2021-05-08.

- [31] G. de Marino. D^0 Lifetime Measurement with Belle II Early Data. Laurea thesis, Pisa U., 2019.
- [32] J. Kandra. Private communication with thesis consultant, 2021.
- [33] F. Tenchini. Vertex Fitting in the Belle II Analysis Framework. *PoS, Vertex* 2016:059, 2017.
- [34] S. Dey and A. Soffer. Beam-Constrained Vertexing for B Physics at the Belle II Experiment. *Springer Proc. Phys.*, 248:411–415, 2020.
- [35] Coadou Y. Boosted Decision Trees and Applications. *EPJ Web of Conferences*, 55:02004–, 07 2013.
- [36] Humair T. et al. Prompt $B^0 \rightarrow J/\psi K_S$ analysis. BELLE2-NOTE-PH-2020-038, unpublished.
- [37] Wolfgang Waltenberger. RAVE—A Detector-Independent Toolkit to Reconstruct Vertices. *Nuclear Science, IEEE Transactions on*, 58:434 – 444, 05 2011.
- [38] Dembinski H. et al. Jupyter-friendly Python interface for C++ MINUIT2 : scikit-hep/iminuit:. <https://doi.org/10.5281/zenodo.4759039>, May 2021. Accessed: 2021-05-06.
- [39] R. Pestotnik et al. The Aerogel Ring Imaging Cherenkov system at the Belle II spectrometer. *Nuclear Instruments and Methods in Physics Research Section A: Accelerators, Spectrometers, Detectors and Associated Equipment*, 876:265–268, 12 2017.
- [40] H. Miyake, R. Grzymkowski, R. Ludacka, and M. Schram. Belle II production system. *Journal of Physics: Conference Series*, 664:052028, 12 2015.
- [41] W. D. Hulsbergen. Decay chain fitting with a Kalman filter. *Nuclear Instruments and Methods in Physics Research Section A: Accelerators, Spectrometers, Detectors and Associated Equipment*, 552(3):566–575, Nov 2005.

List of Figures

1.1	Phase 3 -Total recorded integrated luminosity	5
1.2	Schematic illustration of the accelerator and the Belle II detector	6
1.3	The Belle II detector Coordinate System	7
1.4	The Belle II detector	10
2.1	The Unitarity triangle	12
2.2	Δt fits performed by the Belle collaboration for B^0 and B^+ mesons	16
2.3	Belle Δt fit for both CP final eigenstates and CP asymmetry measurement	17
2.4	Time-dependent flavor asymmetry fit from Belle measurement . .	18
3.1	"IP" constraint for B_{tag} vertexing	21
3.2	"Tube" constraint for B_{tag} vertexing	22
3.3	MC/Data comparison - Summer 2020 tag-side validation	24
3.4	MC/Data comparison - Fall 2020 tag-side validation	26
3.5	MC and data comparison - Summer 2020 signal-side validation . .	27
3.6	MC/Data comparison - tag and signal decay time residual	28
4.1	Δt_{res} fit results - B0toPiDPtoK2Pi	37
4.2	Δt and Δt_{MC} lifetime fit - B0toPiDPtoK2Pi	38
4.3	Δt_{res} fit results - B0toPiDStoK2Pi	39
4.4	Δt and Δt_{MC} lifetime fit - B0toPiDStoK2Pi	40
4.5	Δt_{res} fit results - B0toPiDStoK4Pi	41
4.6	Δt and Δt_{MC} lifetime fit - B0toPiDStoK4Pi	42
4.7	Δt_{res} fit results - B0toJPsiKStoMuMu	43
4.8	Δt and Δt_{MC} lifetime fit - B0toJPsiKStoMuMu	44
4.9	Δt_{res} fit results - B0toJPsiKStoEE	45
4.10	Δt and Δt_{MC} lifetime fit - B0toJPsiKStoEE	46
4.11	Δt_{res} fit results - BPtoJPsiKtoMuMu	47
4.12	Δt and Δt_{MC} lifetime fit - BPtoJPsiKtoMuMu	48
4.13	Δt_{res} fit results - BPtoJPsiKtoEE	49
4.14	Δt and Δt_{MC} lifetime fit - BPtoJPsiKtoEE	50
4.15	Δt_{res} fit results - BPtoPiD0toKPi	51
4.16	Δt and Δt_{MC} lifetime fit - BPtoPiD0toKPi	52
4.17	Δt_{res} fit results - BPtoPiD0toK3Pi	53
4.18	Δt and Δt_{MC} lifetime fit - BPtoPiD0toK3Pi	54
5.1	Time resolution function - fit results and parameter values	58
5.2	Time resolution function - fit results for the c parameter values . .	59
5.3	Time resolution function - fit results for the f parameter values .	60
5.4	Time resolution function - lifetime fit results	60

List of Tables

2.1	τ_{B^0} and τ_{B^+} values measured by the BaBar and Belle experiments for selected final states	15
2.2	Time-dependent CP parameter values measured by the BaBar and Belle experiments	16
4.1	MC Decay Modes used for the analysis	32
4.2	B -meson τ values from a preliminary <code>DeltaT</code> fit	35
4.3	B -meson τ values from a preliminary <code>MCDeltaT</code> fit	35
4.4	# events in the signal MC dataset	36
4.5	Lifetime fit results - New MC Data	55
4.6	B -meson τ values from a <code>MCDeltaT</code> fit	55
A.1	Summary of fit results for the neutral channels	69
A.2	Summary of fit results for the positive channels	69

A. Time Resolution Function and Lifetime Fit - Summary Table

In Chapter 4 the procedure of fitting Δt_{res} variable from simulated MC samples by a proper decay-time resolution function was described. This fit was performed for nine different decay channels, corresponding to neutral B^0 -meson and charged B^+ decay modes. Based on fitted values of eleven free floating parameters, the lifetime fit was performed on `DeltaT` and `MCDeltaT` variable spectra. The results and pictorial illustration of the fitting procedure results are presented and discussed in Chapter 3 and Chapter 4. The Table A.1 and Table A.2 on the following page summarize the determined values of parameters and fitted values of B -meson lifetime across all nine studied channels.

Fitted var.	B0toPiDPtoK2Pi	B0toPiDStoK2Pi	B0toPiDStoK4Pi	B0toJPsiKStoMuMu	B0toJPsiKStoEE
μ	-0.0356 ± 0.0028	-0.0372 ± 0.0048	-0.0367 ± 0.0051	-0.0303 ± 0.0025	-0.0367 ± 0.0032
σ	0.3592 ± 0.0048	0.3557 ± 0.0084	0.3725 ± 0.0085	0.3317 ± 0.0055	0.3312 ± 0.0075
f_M	0.4923 ± 0.0164	0.5444 ± 0.0272	0.4792 ± 0.0286	0.5019 ± 0.0192	0.503 ± 0.0259
f_{TR}	0.3397 ± 0.0091	0.3536 ± 0.0135	0.3261 ± 0.0176	0.3209 ± 0.0079	0.3350 ± 0.0103
f_{big}	0.1878 ± 0.0130	0.2028 ± 0.0194	0.1626 ± 0.0224	0.1888 ± 0.0116	0.1859 ± 0.0150
c_{LMs}	0.9596 ± 0.0226	1.0033 ± 0.0335	0.9287 ± 0.0388	1.0360 ± 0.0230	1.0245 ± 0.0283
c_{RM_s}	1.1502 ± 0.0381	1.2006 ± 0.0544	1.0849 ± 0.0723	1.1950 ± 0.0379	1.2151 ± 0.0466
c_{LB_s}	0.2810 ± 0.0090	0.2944 ± 0.0122	0.2645 ± 0.0176	0.2960 ± 0.0081	0.2800 ± 0.0104
c_{RB_s}	0.3867 ± 0.0120	0.4019 ± 0.0164	0.3499 ± 0.0231	0.3938 ± 0.0110	0.3945 ± 0.0143
b	2.0548 ± 0.0273	1.9904 ± 0.0387	2.0558 ± 0.0469	1.9002 ± 0.0263	1.9 078 ± 0.0387
f_B	0.3230 ± 0.0100	0.3339 ± 0.0159	0.3213 ± 0.0173	0.3398 ± 0.0120	0.3248 ± 0.0161
$\tau_{0/+}(\Delta t)[ps]$	1.532 ± 0.003	1.528 ± 0.005	1.524 ± 0.006	1.530 ± 0.003	1.524 ± 0.004
$\tau_{0/+}(\Delta t_{MC})[ps]$	1.531 ± 0.002	1.531 ± 0.004	1.523 ± 0.005	1.528 ± 0.002	1.523 ± 0.003

Table A.1: Summary of fit results for the neutral channels

Fitted var.	BPtoJPsiKtoMuMu	BPtoJPsiKtoEE	BPtoJPsiKtoMuMu	BPtoJPsiKtoEE
μ	-0.0451 ± 0.0012	-0.0416 ± 0.0017	-0.0490 ± 0.0012	-0.0455 ± 0.0020
σ	0.2912 ± 0.0045	0.2929 ± 0.0062	0.3228 ± 0.0042	0.3287 ± 0.0063
f_M	0.0990 ± 0.0076	0.1070 ± 0.0102	0.1090 ± 0.0065	0.1083 ± 0.0101
f_{TR}	0.3507 ± 0.0070	0.3415 ± 0.0081	0.3877 ± 0.0046	0.3643 ± 0.0084
f_{big}	0.4788 ± 0.0095	0.4985 ± 0.0131	0.5083 ± 0.0074	0.4923 ± 0.0133
c_{LM_s}	0.3586 ± 0.0095	0.3633 ± 0.0116	0.3015 ± 0.0068	0.3235 ± 0.0121
c_{RM_s}	0.3967 ± 0.0133	0.3993 ± 0.0158	0.3508 ± 0.0090	0.3710 ± 0.0161
c_{LB_s}	1.1807 ± 0.0190	1.2333 ± 0.0246	1.0961 ± 0.0124	1.1142 ± 0.0235
c_{RB_s}	1.416 ± 0.0386	1.4257 ± 0.0446	1.3209 ± 0.0214	1.3124 ± 0.0400
b	1.8133 ± 0.0213	1.7575 ± 0.0276	1.8484 ± 0.0151	1.8450 ± 0.0258
f_B	0.6260 ± 0.0164	0.6274 ± 0.02358	0.6894 ± 0.0110	0.6579 ± 0.0179
$\tau_{0/+}(\Delta t)[ps]$	1.644 ± 0.003	1.639 ± 0.004	1.641 ± 0.002	1.644 ± 0.003
$\tau_{0/+}(\Delta t_{MC})[ps]$	1.641 ± 0.002	1.639 ± 0.003	1.639 ± 0.002	1.644 ± 0.002

Table A.2: Summary of fit results for the positive channels